CO_2 degassing of geothermal fluids during coreflood experiments

by:

Cas Verweij

In partial fulfilment of the requirements for the degree of Master of Science in Applied Earth Science at Delft University of Technology

to be defended publicly on
November 4th 2021

Student number:	4371518	
Project duration:	February 1st, 2021 – November 4th, 2021	
Thesis committee:	Dr. A.M.H. Pluymakers,	TU Delft, supervisor
	Dr. C.S. Boeije,	TU Delft
	Prof. P.L.J Zitha,	TU Delft
	Prof. D.F. Bruhn,	TU Delft

An electronic version of this thesis is available at http://repository.tudelft.nl/.

TU Delft

Abstract

In the energy transition from fossil fuels to less polluting renewable energy sources geothermal energy are considered as a promising technology. Gasses such as CO_2 are often dissolved in geothermal waters. With the extraction of these fluids from the reservoir, a change in pressure will occur towards the extraction well which may cause dissolved gas to exsolve. The exsolved gas may clog the pores of the reservoir rock near the extraction well and therefore reduce the effective permeability, which can result in reduced production of geothermal waters. This project is aimed at experimentally investigating the conditions of the onset of the degassing process and what the influence of the degassing process is on the permeability. Therefore Bentheimer and Berea sandstone core flood experiments were performed, using either tap water or brine with different CO_2 concentrations (0.2 - 1.3 mol/L) and at temperatures between 30 and 90°C. Flow rates were varied/kept constant, between 90 - 2 bar and between 5 and 22 bar respectively.

At 30 °C and up to 50 bar the onset of the degassing process is controlled by Henry's law, i.e. it is governed by the solubility of gaseous CO_2. The onset of the degassing process is not influenced by the pore size and initial permeability. At these conditions the effective permeability decreases by a factor 2 to 5 in the Bentheimer sandstone core and by about a factor 10 in the Berea sandstone core. This change in effective permeability is gradual in the Bentheimer sandstone while in the Berea sandstone the change is near-instant. For rocks with small pore sizes and low initial permeability, the reduction in effective permeability is larger and the rate of permeability decrease is faster.

Experiments at temperatures between 30 and 90°C show that with increasing temperature Henry's law becomes increasingly inaccurate to find the onset of the degassing process. The onset degassing pressure increases with temperature but are significantly lower than Henry's law. This inaccuracy can partly be explained by the fluid in the core not reaching the right temperature or by the values used for extrapolating Henry's law for different temperatures. In experiments performed with a 1M NaCl brine the pressure at which the degassing process starts is higher than for experiments performed with tap water. The increased salinity does not influence the change in effective permeability due to degassing. The reason for this is that the change in interfacial tension between CO_2 does not change sufficiently between tap water and Brine to cause differences in the degassing process.

The results obtained from this research can be used for successful management of geothermal projects. It shows at what conditions the degassing process starts and what the effect of this process is. Once the conditions are known they can be avoided. The research also shows the degassing process and its effects can be reversed.

Acknowledgement

During the last nine months I was lucky enough to receive support which enabled me to write this thesis, to these people I would like to express my gratitude. First is wish to thank Michiel Slob for the technical support in the laboratory without which it would not have been possible to do the experiments. Next I would like to acknowledge Willemijn and Wuis for their presence in the lab, which made the quiet corona months more endurable. I would like to thank Anne Pluymakers for her dedicated involvement throughout the process. Pacelli Zitha and David Bruhn I would like to express my gratitude to for taking place in my graduation committee. A special thanks I would like to give to Chris Boeije for the support and help throughout the last months. I really appreciated our weekly meetings in which I could bother you with my questions and problems. Last but not least I would like to thank my friends and family for the support and encouragement.

Contents

List of Figures

List of Tables

1 Introduction

On the 4th of November 2016 the Paris agreement treaty on climate change went into force with the goal to limit global warming. In order to accomplish this goal the emission of greenhouse gases into the atmosphere has to reduce drastically. A transition has to take place from carbon rich fossil fuels to more renewable energy sources (UNFCCC, 2021). Geothermal energy is an important technology in this transition because of its ease of use and competitiveness with conventional fossil fuels (Feili et al., 2013). The technology of extracting hot water from the subsurface can be used directly for heating and cooling purposes. The high temperature geothermal waters can also be used in geothermal power plants for the production of clean electricity.

Since 2005 geothermal energy plays a role in the Netherlands. in this year the first exploration license for geothermal energy was granted. By the year 2020 this first license has grown to 27 operational geothermal production systems that extract heat from the subsurface by producing hot and injecting cooled water (EZK, 2021). The heat that is being produced in the Netherlands is obtained from five geological formations; the lower North Sea group, the upper-Jura/lower-Krijt, the Trias group, the Rotliegend group, And the lower Carboniferous group. Most of these formations are sandstone formations (25/27), except the Carboniferous which is a limestone formation (2/27). The depth from which water is produced from these formations is between 700 and 2800 meters below N.A.P. (EZK, 2021). The temperature of the fluid that is produced is strongly correlated to depth, it increases on average 30 °C per kilometer depth. Besides the temperature the porostiy and permeability are also important since they determine for a large part how much water can be produced (EBN, 2018). The permeability and porosity can differ between formations and even within a formation. One of the targets of geothermal energy in the Netherlands is the Delft Sandstone Member (DSSM) located at two kilometers depth in which there are already two operational geothermal doublets. Water is produced from the aquifer at temperatures between 65 and 75 °C from two sandstone layers with permeabilities between 90 and 290 mD for the lower permeable layer and between 625 and 1130 mD for the higher permeable sandstone layer (Donselaar et al. 2015).

To utilize the geothermal potential of the Dutch subsurface a geothermal masterplan has been created by the Dutch Association Geothermal Operators (DAGO), Stichting Platform Geothermie, Stichting Warmtenetwerk and Energie Beheer Nederland (EBN), supported by the Dutch ministry of Economic affairs and climate and ministry of Internal affairs. The energy that is produced with geothermal in 2018 is 3 petajoule (PJ). The ambition for geothermal energy as stated in the masterplan is to increase this to 50 PJ by the year 2030 and 200+ PJ by the year 2050. To reach these ambitions a significant upscaling in the amount of geothermal doublets is needed, the 27 doublets in 2020 have to increase to 175 by 2030 and 700 by 2050. When successful geothermal energy could contribute 23 % of the total heat demand in 2050 (EBN, 2018). An increase in geothermal doublets and production will also result in more knowledge which will reduce technical risks.

One potential risk originates from minerals and gases (such as CO_2, CH_4, N_2) that are dissolved in geothermal waters. With the production of these waters, a change in pressure and temperature

will occur towards the extraction well. These changes disturb the equilibrium the water is in with its dissolved minerals and gases (Patzay et al., 1998) and can result in various problems, such as the precipitation of minerals and degassing (Blöcher et al., 2016). Degassing is the phenomenon that occurs when a fluid reaches its bubble point due to changes in pressure and/or temperature. At this point the gases dissolved in the fluid will come out of solution. Geothermal waters can have various gases in solution which come out of solution at different pressures/temperatures. The system then goes from single-phase flow (liquid) to two-phase flow (liquid and gas). The effective pore space available for the flow of water is reduced, as part of the total pore space is taken up by gas. Therefore the effective permeability of the liquid phase will reduce (Bear, 2013, p. 195).

One of the places where this might have happened is the Gross Schönebeck geothermal reservoir in Germany. During a period of 2.5 years the productivity index during production reduced non-linearly from 8.9 m^3 /(mMPa) to 0.6 m^3 /(mMPa). Five possible reasons for this reduction in productivity index were found, one of them being a decrease in permeability due to two phase flow (Blocher et al., 2016). The extent of this problem is not fully understood yet and needs to be further investigated and quantified, this leads to the following research question:

"To which extent is the flow of water in rocks limited by release of free gas from a saturated water/gas solution?"

This thesis is aimed at experimentally investigating the conditions at which conditions the onset of the degassing process starts and investigating what the influence of the degassing process is on the permeability. Processes and factors influencing the degassing process and its effect on the permeability will be analyzed and discussed. These factors include the rock pore scale characteristics, temperature, and salinity.

2

Theoretical Background

This chapter provides relevant background information to this project. The first section discusses the governing law of fluid flow through porous media, which is used widely throughout the thesis. The subsequent section discusses how pressure changes throughout a reservoir during production, which is the cause of the degassing of geothermal fluids. The following sections discus different geothermal fluids. Next the solubility of gasses is discussed together with factors that influence it. The penultimate section discusses the trapping of the free gas phase. This chapter is finalized with a pore scale analysis of the two types of sandstones used in the experiments.

2.1. Darcy Law

The governing equation to describe the flow of a fluid through a porous medium is Darcy's law. This law forms the basis for working out the raw data obtained from the experiments. Darcy's law can be written as;

$$q = \frac{Q}{A} = \frac{k}{\mu}\frac{\Delta(P - \rho g z)}{L} \tag{2.1}$$

Where q is the flux, or volumetric flow rate per unit area, defined in the units (*m/s*), Q is the volumetric flow rate (m^3/s), A is the cross-sectional area of the sample (m^2), k is the permeability (m^2), P is the pressure (Pa), ρ is the density (kg/m^3), g is the gravitational acceleration (m/s^2), z is the vertical coordinate (measured downwards) (m), μ is the dynamic viscosity (Pa*s), and L is the length of sample (m).

The gradient of P – pgz can be seen as the driving force for flow in porous medium, since fluid flows from regions of higher energy to lower energy. The permeability is rock property and is independent on the fluid but can vary with stress and temperature. The effect of the fluid on the flow rate is accounted for by the viscosity. Permeability is often displayed in the "Darcy" units.

1 Darcy = 0.987 × 10−12 m^2 ≈ 10−12 m^2.

Darcy's law as written in equation 2.1 is established for the flow of a single-phase fluid through a porous medium (Bear, 2013, p.625). When a fluid degasses and gas comes out of solution there are two phases instead of one. The single-phase Darcy's law does not apply anymore and needs to be modified for the presence of a second phase. For the two immiscible fluids that flow through the porous medium Darcy's law can be extended to describe the flow for each fluid: (Bear, 2013, p.625)

$$q_1 = \frac{k_1}{\mu_1}\frac{\Delta P_1}{L} \tag{2.2}$$

$$q_2 = \frac{k_2}{\mu_2}\frac{\Delta P_2}{L} \tag{2.3}$$

The permeability can be seen as an indication of the ability for a fluid to flow through the rock. The numerical value for the permeability (k) depends on the diameter of the pores in the rock and the interconnectedness of void space (Zimmerman, 2018). It is a characteristic of a rock and therefore is not dependent on the types of fluids that flow through it. In 2.2 and 2.3 k_1 and k_2 are the effective permeabilities of the porous medium to fluids 1 and 2. In this project the focus is on how the flow of water through porous medium is limited by exsolved CO_2. Therefore the effective permeability of through water will be used denoted from this point onward simply by the effective permeability or k_{eff}. Equation 2.2 can be adapted to express k_{eff}:

$$k_{\text{eff}} = \frac{q}{\Delta P}\mu L \tag{2.4}$$

One of the conditions that needs to be met for Darcy's law to be valid is that the fluid flow is laminar. The dimensionless Reynolds number (Re) is used as a criterion to identify laminar flow from turbulent flow (Bear, 2013, p.195). The Reynolds number is defined as:

$$Re = \frac{\rho D_p U}{\mu} \tag{2.5}$$

In which Re is the Reynolds number, μ is the fluid dynamic viscosity in kg/(m*s), D_p is the particle diameter in a packed-bed system in m, U is the fluid velocity in m/s, and ρ is the fluid density in kg/m^3. The particle diameter for a Bentheimer is equal to 0.14mm according to Muljadi et al. (2015).

According to Bear (2013, 0.195) Darcy's law is valid when the Reynolds number is between 1 and 10. These values are not agreed on by all authors. Muljadi et al. (2015) for instance gives a Reynolds number of 0.196 for Bentheimer sandstones, which is lower than conventional values due to tortuosity and non-heterogeneity. Applying Reynolds numbers of 0.196, 1 and 10 to equation 2.5 give flow rates of the transition between laminar and turbulent flow of 85, 434 and 4337 mL/min respectively for a Bentheimer sandstone.

2.2. Pressure dissipation in radial flow

This section of the theoretical background is to show how the pressure profile of reservoir of looks when it is under production. What his shows is that pressure dissipation especially occurs close to the wellbore, therefore this is the location at which the degassing process is expected to take place.

To illustrate the pressure profile of a reservoir often simplification of a circular reservoir with a constant boundary pressure and constant flow rate into the wellbore is used . For this simplification, the reservoir has a constant thickness H fully penetrated with by a vertical well with radius R_W, an isotropic permeability k, an outer radius R_O where the pressure remains undisturbed at P_O. From the wellbore a fluid is produced at a constant flow rate Q. Figure 2.1 shows how the cross sectional view of such a reservoir would look like.

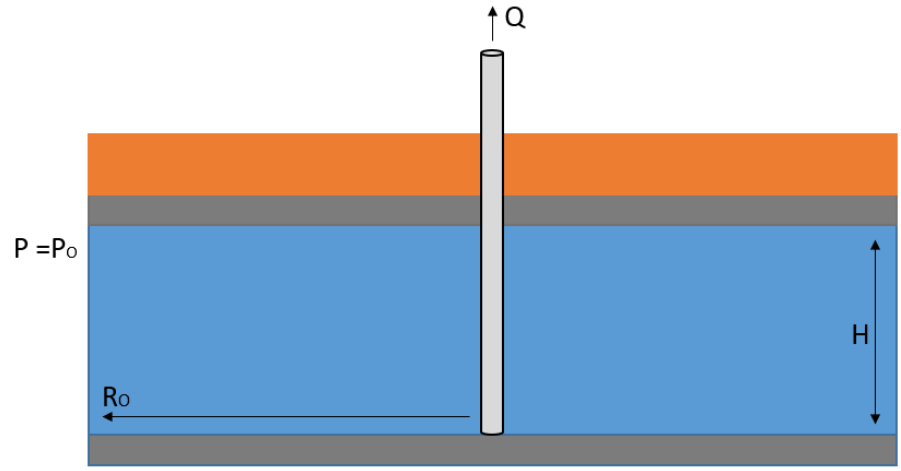

Figure 2.1: Left: cross sectional view or a reservoir with well in place , Right: plan view of a reservoir with radial flow towards the well

Once there is a steady state in the reservoir, pressure does not change over time, the flow rate into the reservoir at R0 is exactly the same as the flow rate at the wellbore R_W. For the flow in the R direction Darcy's law is as follows

$$Q = \frac{kA}{\mu}\frac{dP}{dR} \tag{2.6}$$

The cross-sectional area normal to the flow at a radial distance R form the center of the well is 2πRH

$$Q = \frac{2\pi kH}{\mu}R\frac{dP}{dR} \tag{2.7}$$

Separate the variables, and integrate from the outer boundary, R = R_O, to some generic location R:

$$\frac{dR}{R} = \frac{-2\pi kH}{\mu Q}dP \tag{2.8}$$

$$\int_{R_o}^{R}\frac{dR}{R} = -\int_{P_o}^{P}\frac{2\pi kH}{\mu Q}dP \tag{2.9}$$

$$\ln\left(\frac{R}{R_o}\right) = \frac{-2\pi kH}{\mu Q}(P - P_o) \tag{2.10}$$

$$P(R) = P_o - \frac{\mu Q}{2\pi kH}\ln\left(\frac{R}{R_0}\right) \tag{2.11}$$

The pressure varies logarithmically with distance from the wellbore. Due to this the pressure drawdown is largest close to the wellbore, while further away from the wellbore the pressure changes slowly. The figure below shows the pressure profile in a circular reservoir with steady state flow.

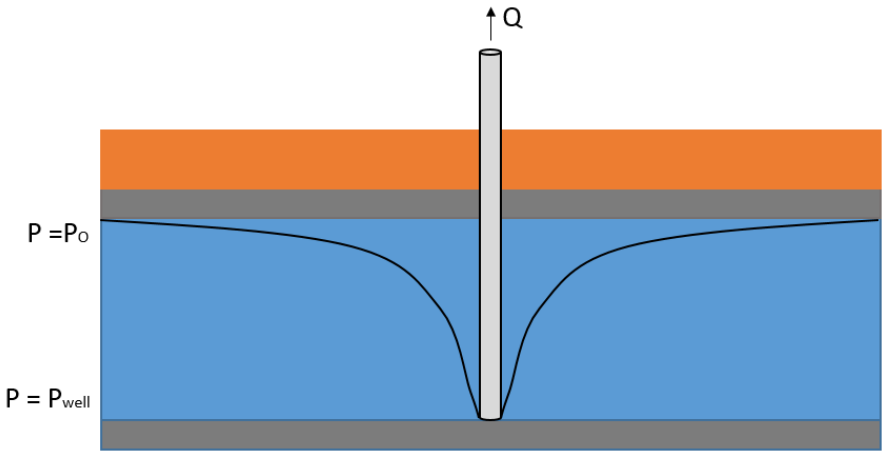

Figure 2.2: Pressure profile of a reservoir with logarithmic pressure dissipation

The figure with the pressure drawdown is a very simplified version of a reservoir with many assumptions being made but it works well as an analogue for a real reservoir. What is especially important to notice from figure 2.2 for this research is the large pressure drawdown close to the wellbore. The amount of pressure drawdown is influenced by both reservoir parameters, such as reservoir permeability and thickness, production parameters, and fluid viscosity. By using equation 2.11 the drawdown can be calculated by entering the values of different parameters. Table 2.1 shows the total drawdown in a reservoir as a function of different parameters using equation 2.11.

Table 2.1: The table displays the parameters that influence the total drawdown in a reservoir with the total drawdown calculated using those parameters using equation 2.11

μ (mpa*s)	0,413	0,413	0,413	0,413
Q (m_3/h)	200	200	200	400
k (D)	0,15	0,15	0,05	0,15
H (m)	50	50	50	50
P_O (Bar)	200	200	200	200
R_O (m)	2500	2500	2500	2500
Bottomhole pressure (Bar)	161,5	190	83,3	180,7
Total drawdown (Bar)	**38,5**	**10**	**115**	**19,3**

2.3. Geothermal fluids

Subsurface waters with a potential for use as a geothermal source often are saturated with minerals and gases. The amount of gases dissolved can vary a great deal as can be seen in the table below in which the dissolved gas concentrations are displayed as measured by various authors at different locations throughout the world. Average CO_2 concentrations for geothermal waters are between 114 and 227 mmol/L according to Haizlip et al. (2016), which is significantly lower than the concentrations they found in Western Turkey.

Table 2.2: CO2 and N2 gas concentrations found by various authors

	Banas et al. ,2007	Regenspurg et al., 2010	Jacobo, 2003	Arnorsson & Gunnlaugsson, 1985	Haizlip et al. ,2016
Component	mmol/L	mmol/L	mmol/L	mmol/L	mmol/l
CO2	2.16	0.22 – 2.08	3.49-37.91	497	340 - 772
N2	4.3		0.07-0,75	22.8	

The hot water that is being produced from the subsurface contains salts, therefore they are often called brines. The amount of salt that is dissolved can differ a lot. Table 2.3 shows the amount of

chloride and natrium that is found in Dutch geothermal wells for three different geological formations. In the Dutch subsurface the largest amount of salt in geothermal water can be found in the Rotliegend with a concentration of 195 g/L. Outside of the Netherlands even higher concentrations can be found, in the Gross Schönebeck in Germany concentrations of 265 g/L can be found (Blocher et al., 2016).

The presence of salts decreases the solubility of gases compared to pure water (Schumpe, 1993, p. 154). When salts are dissolved in water the ionic strength of solution increases and the solubility to other ionic compounds decreases due to a decrease in availability of water molecules. The decrease in solubility is especially large for compounds that are sensitive to ionic strength (Chang Thoman, 2014, p. 287). Therefore it is expected that in fluids with a high salt concentration less carbon dioxide can be dissolved at the same pressure than fluids with a low salt concentration.

Table 2.3: Concentration of compounds in the formation water of Dutch geothermal wells in mg/L, Source: TNO (2016)

	Cl	Na
Jurrasic/Cretaceous	63182	29914
Rotliegend	131669	64088
Carboniferous	48000	23800

2.4. Solubility of gasses and Henry's law

When production starts in a reservoir, geothermal waters move through the reservoir in the direction of the wellbore. As discussed in the previous section, the pressure drawdown close to the wellbore is the largest. This means that as the brine moves towards the production well the CO_2 saturated fluid is depressurized. This causes the solubility of CO_2 to decrease and for the gas to exsolve from solution and form a separate phase.

The solubility of gases in water can be described using Henry's law. This law states that the amount of gas that can be dissolved into a liquid is proportional to the partial pressure of the gas phase. Henry's law constant expresses the proportionality factor of gas at standard conditions of 298.15 K for a range of pressures.

$$H^{cp} = \frac{c_{\mathrm{a}}}{p} \tag{2.12}$$

The SI unit for H^{cp} is mol/L*atm, C_a is the concentration of a gas in aqueous solution in mol/L, and p is the pressure in atm (Sander, 2015). C_a is the maximum solubility of a gas in aqueous solution this is similar to solubility (S in mol/L) which will be used from this point forward instead of C_a.

The solubility of gases decreases with increasing temperatures. For other temperatures than standard conditions of 298.15 K, Henry's law constant can be calculated using formula 2.13. This formula uses the Van 't Hoff equation, which describes the temperature dependence of equilibrium constants.

$$H(T) = H^{\circ} \exp\left[\frac{-\Delta_{\mathrm{sol}} H}{R}\left(\frac{1}{T} - \frac{1}{T^{\circ}}\right)\right] \tag{2.13}$$

H(T) is the Henry's law constant at the required temperature T, H^0 is Henry's law constant at reference temperature T^0 of 298.15 K, $\Delta_{sol}\, H$ is the enthalpy of dissolution that is independent of temperature (Sander, 2015). Table 2.4 shows the Henry's law constant at different temperatures extrapolated using the Van 't Hoff equation, these constant can be used to shows Henry's law at different temperatures (figure 2.3).

Table 2.4: Henry's law constant for different temperatures

T (°C)	H (mol/L*atm)
30	0.031
40	0.024
50	0.019
60	0.015
70	0.012
80	0.010
90	0.008
100	0.006

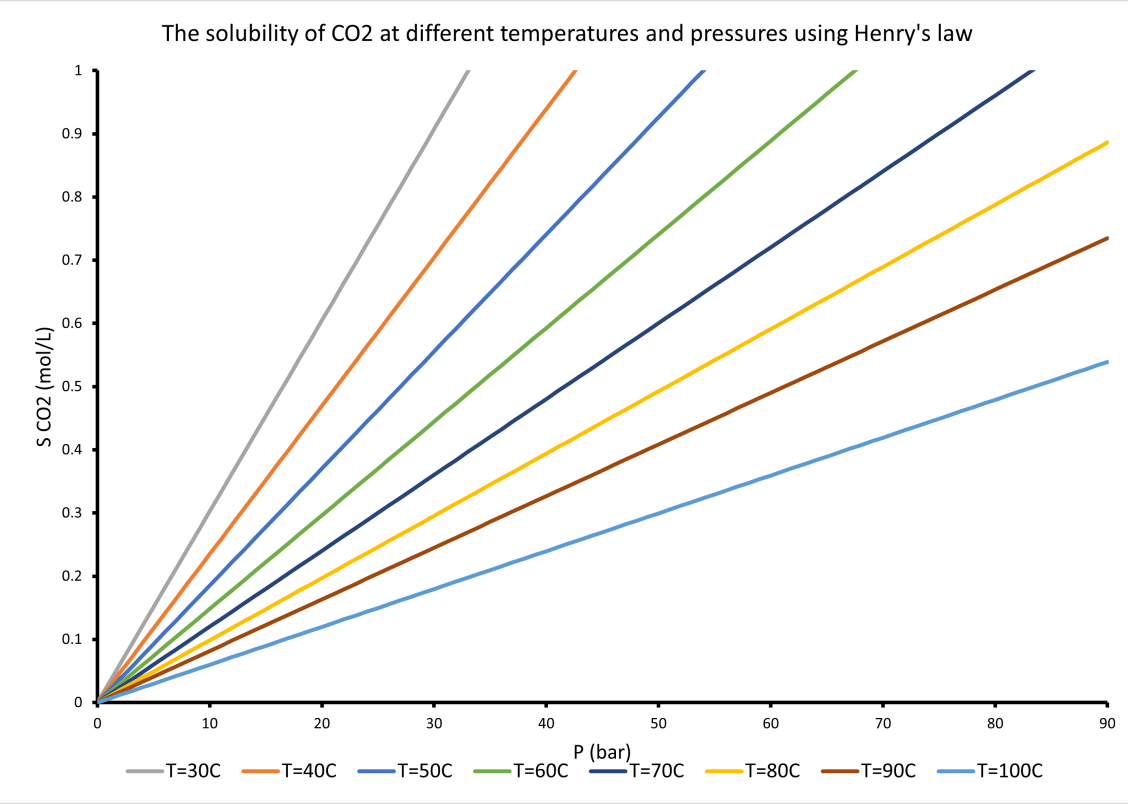

Figure 2.3: Plot of Henry's Law at different temperatures. Constants used are given in Table 2.4. S CO_2 is the maximum solubility of CO_2 according to Henry's law

2.5. Trapping of gasses

During the migration of gas bubbles, the bubbles can either move through the pore network and escape the reservoir through the wellbore, get trapped in the pore network, bubbles can merge with each other to form a larger gas bubble (Mahabadi, 2018). Multiple factors can influence the behaviour of a bubble in a porous medium such as the size of the bubble at nucleation, the merging of bubbles while migrating, the bubble generation rate, and the pore-scale characteristics of the reservoir.

Trapping of exsolved CO_2 bubbles is largely controlled by the wettability of the reservoir rock since it determines the fluid distribution on pore scale (Pentland et al., 2011). For saline aquifer systems the reservoir rocks can be considered to be water-wet for a wide range of reservoir conditions (Al-Menhali Krevor, 2016). Bubbles can get stuck in a pore when the size of the bubble exceeds the radii of the pore throats connected to that pore. Bubbles can be immobilized due to capillary forces locking bubbles in place at the pore scale, therefore preventing the movement of the bubbles in the reservoir (Wildenschild, et al., 2011). In order to migrate and squeeze through the pore throat, the viscous forces moving

the bubble in the direction of the well have to exceed the capillary forces trapping the bubble in the pore (Bear, 2013, p.606).

Figure 2.4 shows the migration of a bubble through a porous medium with the process that influence the trapping of bubbles. The left hand side of the figure shows a gas bubble migrating through the porous medium. The bubble first goes through a pore throat that it can pass due to the bubble radius being smaller than the pore throat radius. The bubble then gets trapped before a pore throat, of which an enlargement in seen on the right hand side of the figure. On this bubble the forces are displayed that control whether a bubble gets trapped, the viscous and capillary forces, together with the variables that influence these forces, the interfacial tension and pore throat radius.

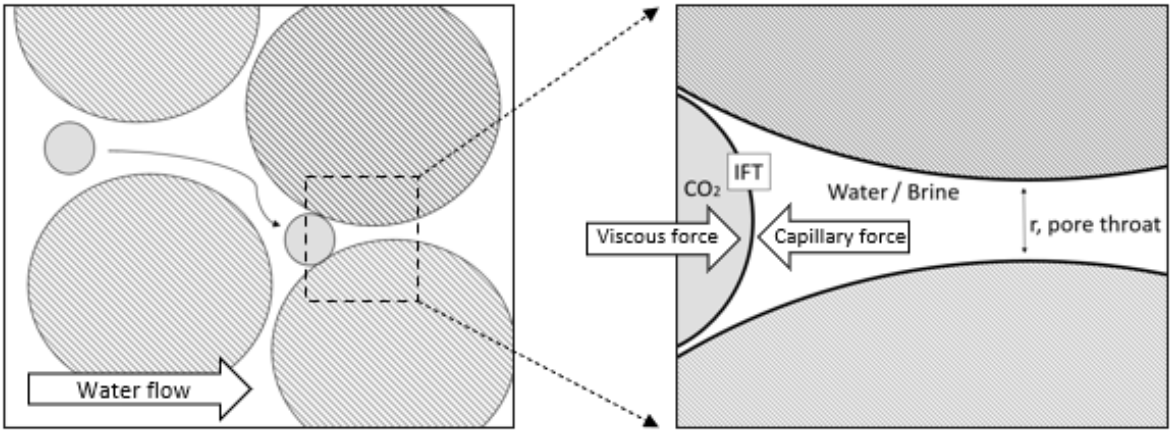

Figure 2.4: Left: A porous medium with a bubble migration through the medium until it gets trapped. Right: trapped bubble with forces acting on the bubble

The capillary force can be seen as a measure of the pores to attract the wetting phase and reject the non-wetting phase (Bear, 2013, p.608). The capillary pressure depends on the interfacial tension between the wetting and non-wetting phase, wettability, and pore scale geometry (equation 2.14).

$$Pc = \frac{2\sigma}{r} cos\theta \tag{2.14}$$

In which Pc is the capillary pressure. θ is the contact angle and determines the wettability of a reservoir. For water wet reservoir the contact angle is smaller than 90°to water. σ is the interfacial tension. When two immiscible fluids are in contact with each other there is a tension at the interface between the two fluids is the interfacial tension (Fanchi, 2002). This tension arises due to a difference in intermolecular forces acting on molecules on the outside of a liquid and in the bulk of the liquid. The effect of this is that there is a net inward force toward the bulk of the liquid for each of the two immiscible fluids (Chang, p.851). The interfacial tension is dependent on temperature (Bear, 2013, p.604). The interfacial tension between CO_2 and water decrease slowly with increasing temperature (Chiquet et al., 2007). The interfacial tension between CO_2 and water increases slightly with increasing salinity of the water (Chiquet et al., 2007). The cappilary force increases with increasing interfacial tension. r is the dependency of the capillary pressure on the pore scale geometry and can be expresses by a pore-size distribution (Bear, 2013, p.608).

The viscous force is the force that opposes the relative motion of two fluids in motion. Viscous force can be seen as the friction force between two surfaces while viscosity can be seen as fluid friction (Arfken, 2012, p. 320). For Darcy's law to be valid, there is assumed to be laminar flow. For laminar flow the viscous forces are higher than inertial forces (Ramsey, 2019). If a CO_2 bubble is trapped by capillary forces the viscous force exerted by the motion of water oppose this force. The viscous force is dependent on the temperature since both the viscosity of CO_2 and water change with temperature. The viscosity of water and CO_2 at different temperatures is shown in table 2.5.

Table 2.5: Viscosity of water and CO_2 with temperature (°C)

T (°C)	Viscosity water (mPa S)	Viscosity CO_2 (mPa S)
10	1.3065	0.014
20	1.0035	0.015
25	0.8927	0.015
30	0.8007	0.015
40	0.6579	0.016
50	0.5531	0.016
60	0.4740	0.017
70	0.4127	0.017
80	0.3643	0.018
90	0.3255	0.018
100	0.101	0.019

A bubble can also get trapped upon nucleates when the bubble radius upon nucleation is larger than the radii of the pore throats connected to the pore space. The larger the bubble radius upon nucleation, the larger the chance of being trapped in the pore and resulting in a higher trapped bubble fraction. Whether a bubble gets trapped at nucleation thus depends both on the nucleation size of the bubble and on the connecting tube radii (Mahabadi et al., 2018).

The trapping of a bubble causes the hydraulic conductivity of the tubes connected to the pore to decrease. The more gas gets trapped in the pore-network, the more the hydraulic conductivity of the pore-network decreases. Muhabadi et al. (2018) shows that the bubble radius has a large influence on the hydraulic conductivity. The hydraulic conductivity starts to decrease rapidly when the bubble radius is near the average of the tube radius.

2.6. Pore scale analysis

The degassing experiments done to explore the research question were either done on a Bentheimer or on a Berea sandstone core, with each of them having their distinct characteristics. In this subsection these characteristics are discussed on pore scale level.

Gong, Nie, and Xu (2020) have performed geometrical and topological analysis of pore spaces for multiple types of sandstones, including the Bentheimer and the Berea sandstone. Figure 2.5 shows a 3D representation of the pores and throats of the Bentheimer and the Berea sandstone. With this pore network model (PNM), in which spheres and cylinders represent the pores and throats, the geometric properties can be analyzed. For the PNM displayed, the Bentheimer has a porosity of 21.79% and an average pore radius of 31 micrometers, the Berea has a porosity of 19.65% and an average pore radius of 22 micrometers.

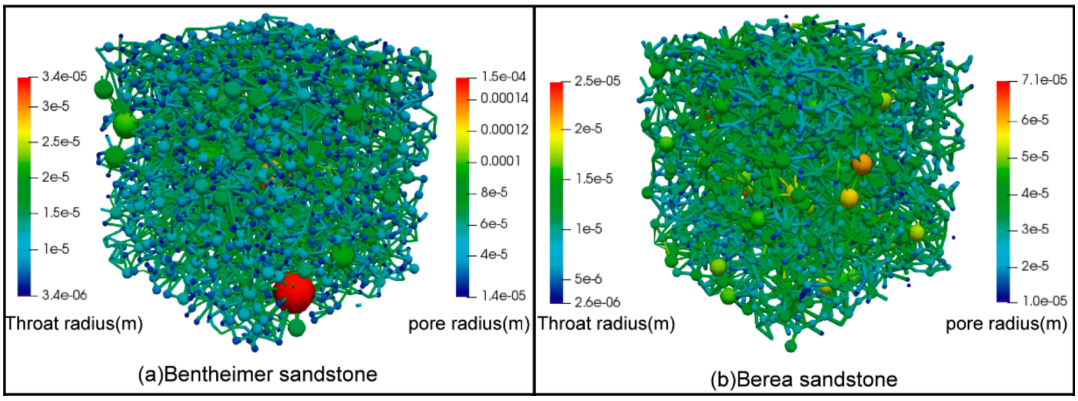

Figure 2.5: Pore network model of Bentheimer (left) and Berea (right),(Gong, Nie, Xu, 2020)

A further pore size distribution indicates that the Bentheimer sandstone has a much wider range of pore sizes than the Berea. For the Bentheimer the pore body radius ranges between 10 and 160 micrometers, while for the Berea this is between 5 and 75 micrometers.

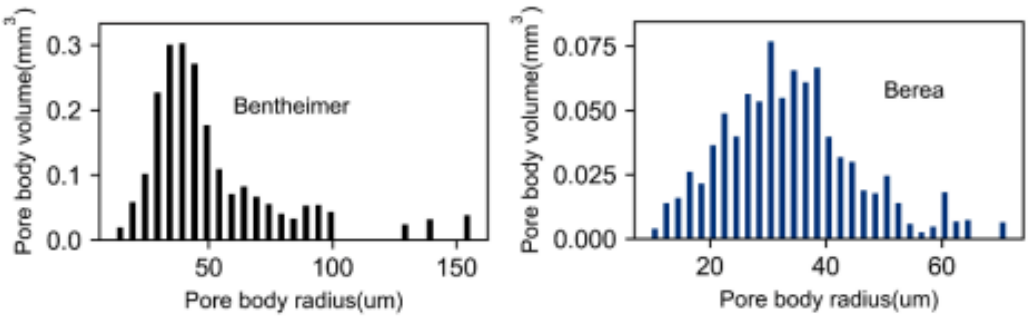

Figure 2.6: Pore body volume distribution of Bentheimer (left) and Berea (right) sandstones,(Source: Gong, Nie, Xu, 2020)

From the PNM also the average pore-throat aspect ratio was analyzed for the Bentheimer and the Berea. This parameter is used to characterize the degree of homogeneity of the pore system. It is the ratio between the average pore size and the average pore throat size. A larger value for this parameter can be an indication for more poor connectivity. The pore-throat aspect ratio for Bentheimer is 1.812 and 1.893 for Berea, this shows that the Berea has a slightly poorer connectivity. With the ratio and the average pore radius also the average pore throat radius can be calculated, which is 17.1 microns for the Bentheimer and 11.6 microns for the Berea (Gong, 2020).

This data shows similarities to pore throat radius distribution obtained from Al-Shakry et al. (2019) as shows in figure 2.7. Their distribution shows that the average pore throat size for Bentheimer sandstones is significantly larger as the Berea sandstone. With the average pore throat radii for Bentheimer being 15 micrometer and for the Berea 6 micrometers. These numbers are lower than the numbers from Gong (2020) but they are similar in showing that the pore throat radii for Bentheimer sandstones are significantly larger than for Berea sandstones.

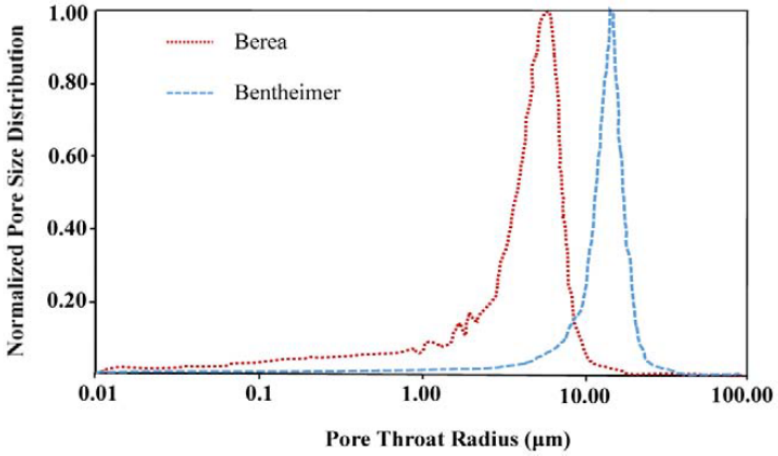

Figure 2.7: Pore throat distribution of Berea and Bentheimer sandstones (Source: Al-Shakry et al. 2019)

Based on literature Al-Shakry et al. (2019), Gong, L (2020) the variability in Bentheimer is relative small, the porosity values of measured for the Bentheimer in these articles are 0.226-0.241 and 0.218 respectively. This is within the same range as the porosity value measured for the Bentheimer at the TU Delft by Peksa et al. (2015) of 0.200-0.260. The porosity values for the Berea sandstone in literature of Al-Shakry et al. (2019) and Gong, L (2020) are 0.178-0.183 and 0.196 respectively. These values are close to porosity values measured at TU Delft by Gong, J et al. (2019) of about 0.2. Because of the low variability in porosity values between literature and what has been measured at TU Delft the

pore data from Al-Shakry et al. (2019) and Gong, L (2020) are assumed to be valid for the samples used in this study.

3

Methodology

Several sets of coreflood experiments were performed in which CO_2 was co-injected with either tap water or a 1M NaCl brine solution. The cores on which these experiments were performed were either a high permeability Bentheimer sandstone core on a lower permeability Berea sandstone core. In this section first the experimental setup which has been used for these experiments will be described. Second the materials that were used in the experiments will be described. Finally the experimental procedures that were followed during the experiments and in the editing of the data will be described.

3.1. Experimental setup

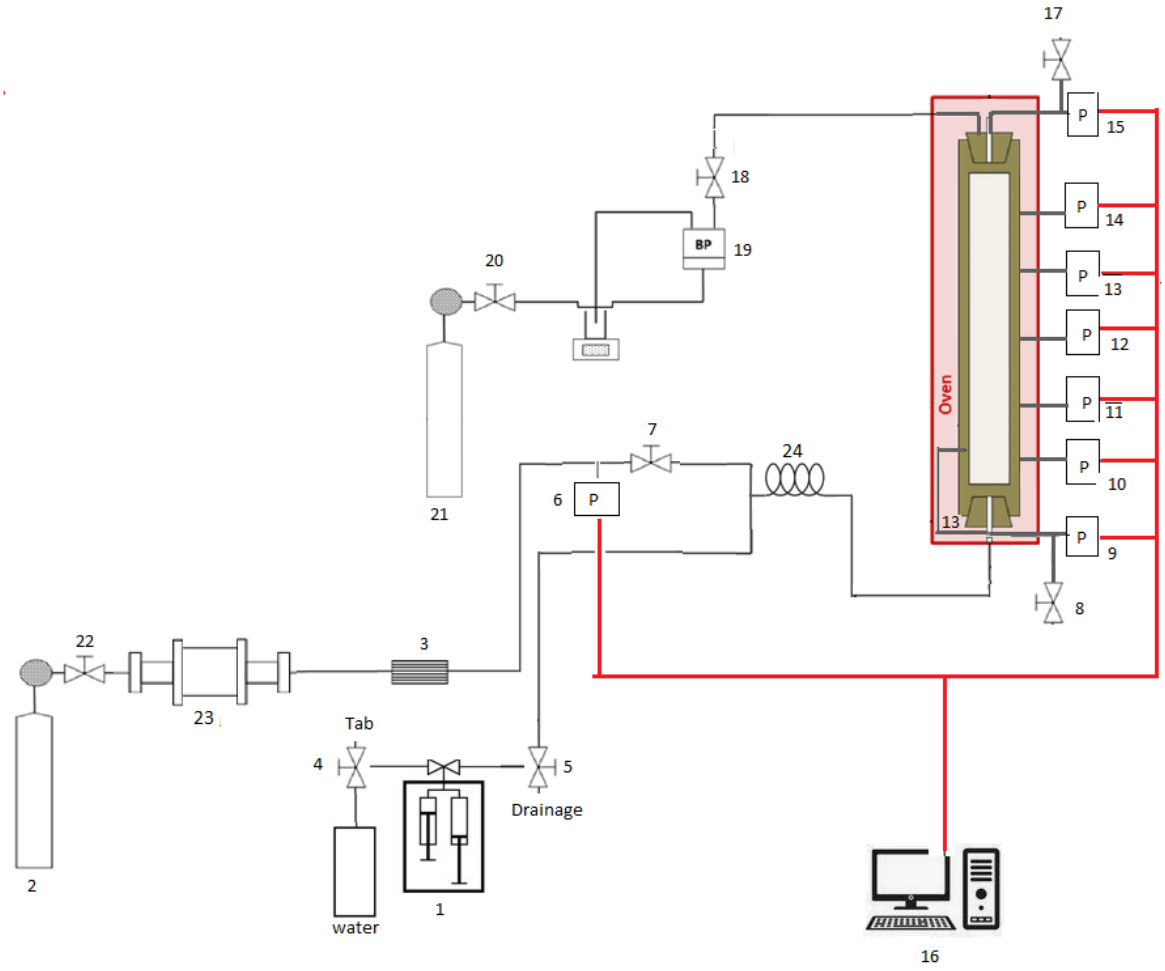

Figure 3.1: Schematic overview of the experimental set-up. 1: Quizix pump, 2: CO_2 cylinder, 3: mass flow controller, 4/5/7/8/17/18/20/22: valves, 6/9-15: pressure transducers, 16: computer, 19: Backpressure, 21: Nitrogen tank, 23: gas booster

Core flood experiments were performed in the experimental setup displayed in figure 3.1. Either a Bentheimer sandstone or a Berea sandstone was placed vertically in core holder made of polyether ether ketone, with the inlet at the bottom of the core holder and the outlet on the top. The cores used had a length of 39 centimeters and a diameter of 4 centimeters. Along the long side of the core a layer of glue is administered. Five holes were drilled in each core at an equal distance from each other in order to measure the pressure on the core. The confining pressure was set equal to the inlet pressure in all experiments performed. A dual cylinder Quizix pump (1) (Quizix QX-1500) was used for the injection of aqueous solutions into the core at a maximum flow rate of 200 mL/min (±0.1 % accuracy). On the inlet side of the pump, it can either take water straight from the tap or from a pre-prepared solution. A mass flow controller (3) (Bronkhorst, EL-FLOW,) was used to regulate the amount of gas injected during co-injection, the range of the mass flow controller is between 1.2 and 60 g/hour (±0.5 % accuracy). During the first three sets of experiments the mass flow controller was directly attached to a CO_2 tank (2). In the later sets of experiments the pressures that needed to be reached exceeded the maximum pressure that could be obtained with the CO_2 tank. Therefore a gas booster was placed before mass flow controller in order to be able to inject gas till pressures up to a 100 bars. Seven pressure transducers (6.9-15) (Keller PA-33X with ±0.5 % accuracy) were installed along the core, 5 of them at an equal distance on the core, and one on each side of the core. The transducers were linked to a computer (16) on which the pressure can be monitored during the core flood experiments. The computer recorded the data from the transducers with a 2 second time interval. The pressure on the

outlet of core was set using a backpressure regulator (19) attached to a tank of nitrogen (21). The core holder with core was placed in an oven to allow for a constant temperature.

3.2. Materials

In this study core flood experiments were carried out on a Bentheimer sandstone core and on a Berea sandstone core.

Bentheimer sandstone is a shallow marine formation deposited during the lower Cretaceous. Its lateral continuity and block scale homogeneous nature, together with constant grain size distribution, porosity, permeability and dielectrical values, make it an ideal rock for laboratory studies. The mineralogy of Bentheimer sandstone consists largely out of quartz (91.70 wt %), feldspars (4.86 wt %) and clay minerals (2.68 wt %) ((Peksa, Wolf, Zitha, 2015). The permeability of the core used in experiments was determined in a single phase water injection experiment.

The Berea sandstone is a medium to fine grained sandstone from the Devonian era (PEPPER, De WITT, DEMAREST, 1954). Its properties can vary widely, with porosity ranging between 13-22 % and permeability between 50 and 1000mD. The mineral composition of the Berea sandstone also has some variation but consists mainly of quartz (80-90 wt%), feldspars (4-5 wt%), and clay minerals (2-8 wt%) (Dawson, Pearce, Biddle, Golding, 2015).

The first 5 sets of core flood experiments were done with tap water. Tap water was used instead of demineralized water to prevent the dissolution of clay particles from the cores. The last set of core flood experiments was done using a 1 mol/L NaCl solution. For the brine solution 58.44 grams of NaCl was dissolved in demineralized water which was subsequently degassed.

3.3. Experimental procedure

In this section the procedures for the different experiments will be discussed. For each core a permeability test has been conducted to precisely measure the permeability of core and for the different intervals of the core. Six sets of experiments were conducted to evaluate the onset of the degassing process and its effect on the effective permeability. The first two sets were conducted on a Bentheimer sandstone core and the final four on a Berea sandstone core.

3.3.1. Procedure permeability test

Single phase water injection experiments are used to determine the permeability of the core using Darcy's law (equation 2.1). The permeability is calculated by injecting water through the core at different flow rates and measuring the pressure drop over the different intervals along the core under steady state conditions. By plotting q/A vs $\Delta P/\mu L$ the slope of the line represents the permeability of core. This can be done for each interval of the core to calculate the permeability for every interval. At higher flow rates the point might deviate from this straight line. At the point it starts to deviate the flow in the core is transitioning from laminar to turbulent flow.

In order to determine the permeability of the Bentheimer core, three single phase water injection experiments were performed. First with a backpressure of 10 bars while starting at a low flow rate and increasing the flow rate in steps, a second time with a backpressure of 30 bars while increasing the flow rate, and a final time with a backpressure of 30 bars while starting at a high flow rate and decreasing the flow rate in steps. For the Berea sandstone core two single phase water injection experiments were performed at two different backpressure of 20 and 30 bars.

3.3.2. Argumentation variables co-injection experiments

In order to assess the onset conditions of the degassing process, its effect on the permeability, and the factors that influence the process a total of six sets of experiments have been performed. A single set consists out of multiple experiments that have a common variable (e.g. temperature, CO_2 concentration, salinity) that influences the degassing process. By comparing two or more sets the influence of this variable on the degassing process can be assessed. In the next section the argumentation for the

different variables are explained which are shown in table 3.1.

Between the first and the later five sets of experiment the procedure that was followed was changed. In the first set the CO_2 concentration was increased at a set backpressure in order to find the CO_2 at which the degassing process would start at a set pressure. In the later five sets of experiments the backpressure was lowered in experiments performed with a set CO_2 concentration in order to find the pressure at which the degassing process would start for a set CO_2 concentration. The procedure of lowering the pressure during the experiment was chosen for this set and the following sets because this procedure better conforms what goes on in a reservoir than the procedure in the first set. With production in a reservoir the pressure that a fluid is under decreases as it moves towards the well, lowering the backpressure mimics this decrease in pressure as happens in a reservoir. A similar procedure as used by Zuo Benson (2013) in which a brine/CO_2 solution was depressurized during coreflood experiments.

The first two sets of experiments were performed using a Bentheimer sandstone core and the later four using a Berea sandstone core. As discussed in the previous chapter, the Bentheimer core and the Berea core have very different characteristics. The Bentheimer is ideal for laboratory studies due to its homogenous nature (Peksa et al., 2015). The Berea core was used for the later sets because its permeability is a good fit to the Delft Sandstone Member. The Bentheimer has a high permeability and pore throats that are relatively large compared to the Berea. The lower permeability of the Berea in comparison to the Bentheimer also has the upside that it results in a larger pressure drop over the core through which it is easier to distinguish when the degassing process starts and what the effects are. The parameters for sets two and three are identical except the core that was used. By comparing these two the influence of the pore scale characteristics can be determined.

The fourth set was performed at different temperatures between 30 and 90 °C to assess the influence of temperature on the degassing process. The parameters for sets two and three are identical except the temperature that was set. By comparing these two the influence of the temperature can be determined.

To assess the influence of salinity on the degassing process the fifth and sixth set can be compared. The sixth set was performed using a 1M NaCl brine instead of tap water, the other parameters were identical to the fifth set.

Table 3.1: Parameters used in the sets of experiments

Set	Rock	Water	T (°C)	Flow rate (mL/min)	Concentration (mol/L)	Backpressure (bar)
1	Bentheimer	Tap	30	60	0 - 0.75	5.3 - 21.7
2	Bentheimer	Tap	30	5 -20	0.3 -1.3	50 - 1
3	Berea	Tap	30	15	0.3 - 1.3	45 - 1
4	Berea	Tap	30 - 90	15	0.4 and 0.2	50 - 1
5	Berea	Tap	70	15	0.2 - 0.9	80 - 2
6	Berea	1M NaCl Brine	70	15	0.2 - 0.8	80 - 2

3.3.3. Procedure co-injection experiments

Six sets of experiments were performed. Between each set the core is flushed with CO_2 to drain the water from the core, subsequently the core is flushed with helium to displace the CO_2. Next the core is connected to a vacuum pump to create a vacuum and get all the gas out. When there is a vacuum in the core, water is slowly pumped in the core until water is observed at the outlet of the system. The vacuum makes sure the system is fully saturated with water and is ready for a new set of experiments.

Between each experiment within a set the core is flushed to get the remaining CO_2 out. This is done by first lowering the backpressure, this causes gas expansion and gas to leave the core. Subsequently the backpressure is increased which results in a higher CO_2 solubility in water through which the remaining CO_2 is removed from the core. In the next paragraphs the procedure for each set is given.

Set1: Constant flow rate and backpressure, increase in CO_2 concentration.

This set of experiments were performed at a constant backpressure, a constant temperature of 30 degrees Celsius and a constant flow rate. The experiments in this set has been conducted at a different backpressure value ranging between 5.3 and 21.7 bar. The variable that was varied during each experiment is the CO_2 concentration. With the mass flow controller the CO_2 concentration is stepwise increased from 0 to 0.75 mol/L. When a steady state was reached at a certain CO_2, the CO_2 concentration was increased in to the a higher CO_2 concentration. When increasing the CO_2 concentration the maximum solubility of the gas will be reached and degassing of CO_2 from the fluid will occur in this way the conditions of the degassing process can be found.

Set2: Constant flow rate and CO_2 concentration, decrease in backpressure.
The second set was performed at a constant temperature of 30 degrees Celsius, at constant flow rates between 5 and 20 mL/min and CO_2 concentrations between 0.3 and 1.3 mol/L while gradually decreasing the backpressure. When lowering the backpressure the CO_2 in the core will start to exsolve, which should result in an increase in pressure gradient. For each experiment in this set a different CO_2 concentration was used.

Set3: Difference Bentheimer and Berea sandstone core.
The difference with the second set of experiments is that instead of a Bentheimer sandstone core, a Berea sandstone core was used. The third set of experiments was performed at a constant temperature of 30 degrees Celsius, at constant flow rates of 15 mL/min and CO_2 concentrations between 0.3 and 1.3 mol/L while gradually decreasing the backpressure. The CO_2 concentration used was different for each experiment in this set.

Set4: Effect temperature on degassing process.
The fourth set of experiments was performed at different temperatures ranging between 30 and 90 °C. The experiments were performed by co-injecting tap water at a rate of 15 mL/min and CO_2 at a constant concentration of either 0.4 or 0.2 mol/L while gradually decreasing the backpressure. At least 12 hours before an experiment the temperature of the oven was set to to the temperature that experiment would be performed at, this would allow the core and the metal spiral in front of the core to heat up to the required temperature.

Set5: Degassing conditions process at 70°C with Berea core.
The fifth set was performed at a constant temperature of 70°C, at constant flow rates of 15 mL/min and CO_2 concentrations between 0.2 and 0.9 mol/L while gradually decreasing the backpressure. The CO_2 concentration used was different for each experiment in this set.

Set6: Degassing experiments with brine solution at 70 °C
The sixth and final set of experiments was performed using 1M NaCl brine, at a constant temperature of 70°C, at constant flow rates of 15 mL/min and CO_2 concentrations between 0.2 and 0.8 mol/L while gradually decreasing the backpressure. The CO_2 concentration used was different for each experiment in this set.

3.3.4. Data processing

Due to the procedural differences as described above, the first set of experiments is also processed differently from the other sets.

Set 1.
The raw data obtained from the experiments from the set are the pressures measured at each pressure transducer taken every two seconds during the experiment. The difference between two adjacent pressure transducers combined with the difference in height gives the pressure gradient over an interval. A representative example of raw pressure data obtained from an experiment is shown in figure 3.2.

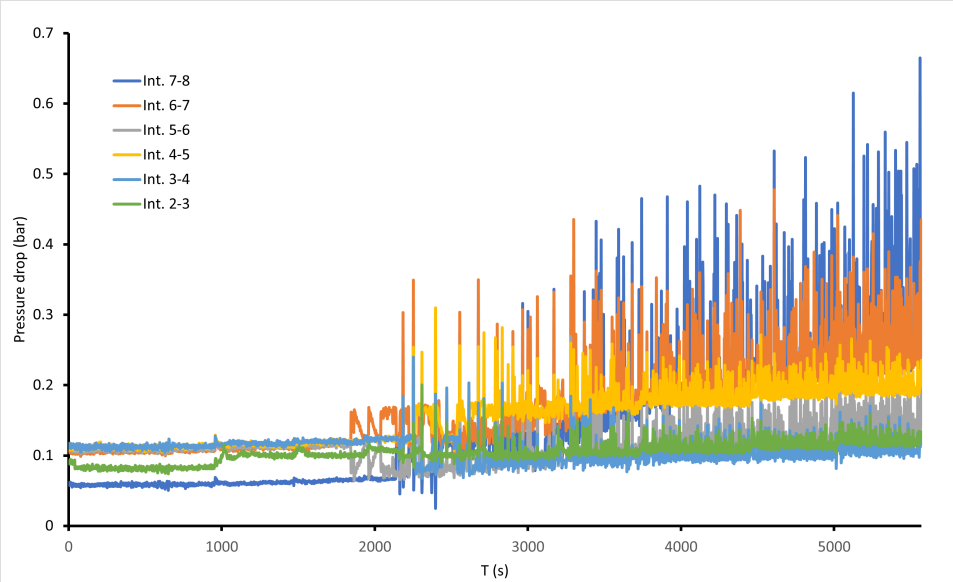

Figure 3.2: Raw data from experiments

The raw data is rather noisy and therefore has to be edited in order to get more clear data. By using time-averaging the signal to noise ratio of the data can be increased. By averaging the data over 20 points, the signal to noise ratio is improved (figure 3.3).

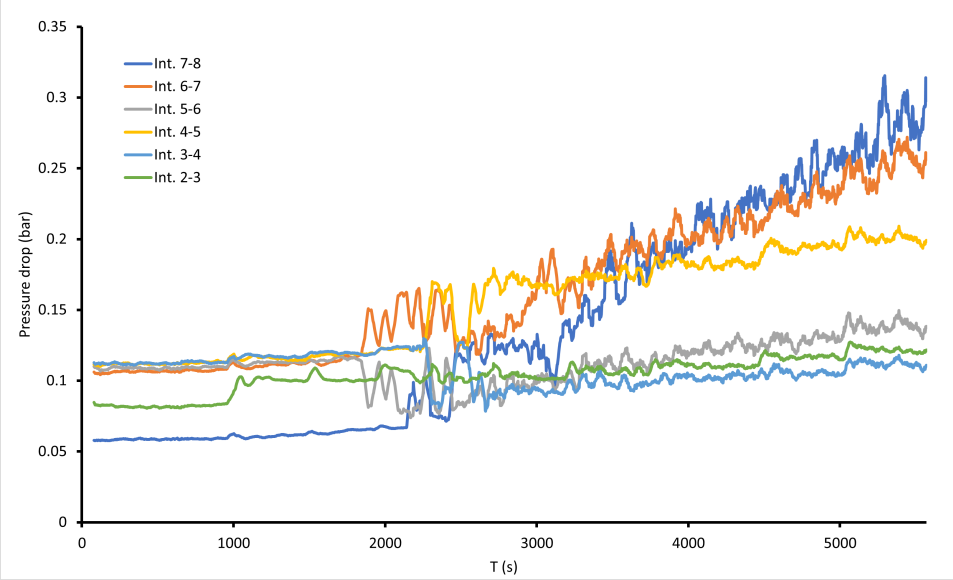

Figure 3.3: Smoothed data after time averaging

The horizontal axis has to be altered to display the CO_2 concentration instead of time. By taking the pressure gradient when steady state is reached for each step, the pressure gradients can be set out against CO_2 concentration as can be seen in figure 3.4.

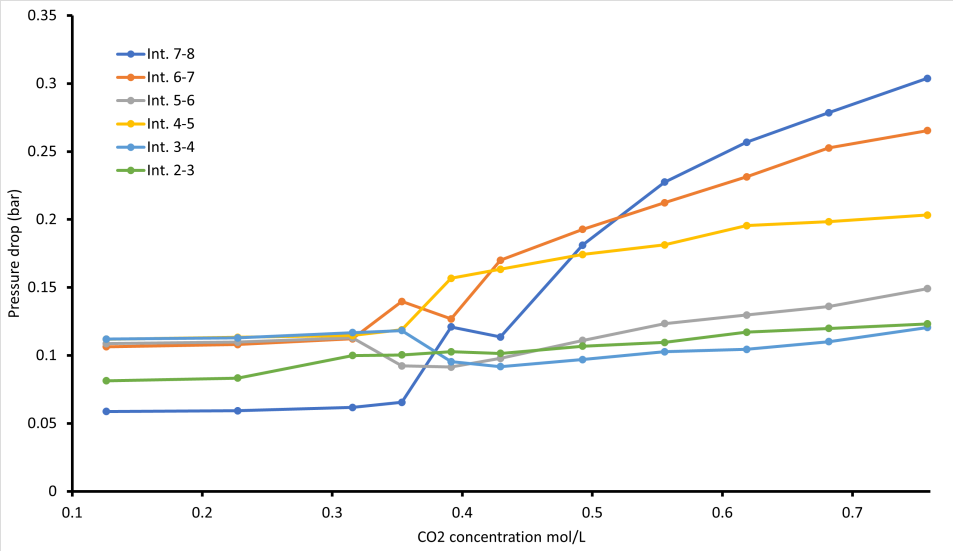

Figure 3.4: Time averaged pressure drop set out against CO2 concentration

Set 2-6.
The experimental procedure for sets 2 to 6 are the same, thus the same data analysis procedure can be used throughout these sets. The raw data for these sets are the same as the first set; pressures measured at each pressure transducer taken every two seconds, with pressure difference between adjacent transducers yielding pressure gradients in a specific section of the core. Figure 3.5 shows a representative example of raw pressure data obtained from an experiment.

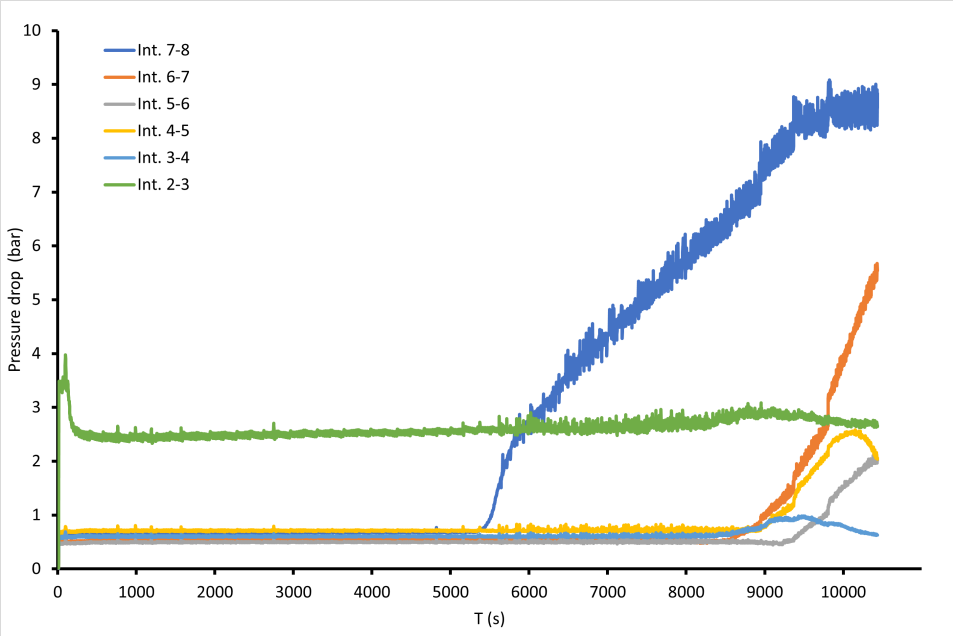

Figure 3.5: Raw data from experiments

The data analysis is similar to the first set; the signal to noise ratio is improved by averaging the data over 20 points. The pressure drop over the last interval is consequently plotted on the vertical axis versus the backpressure pressure on the horizontal axis, as can be seen in figure 3.6. The moment at which the pressure drop over the last interval starts to increase rapidly can be seen as the onset of the degassing process.

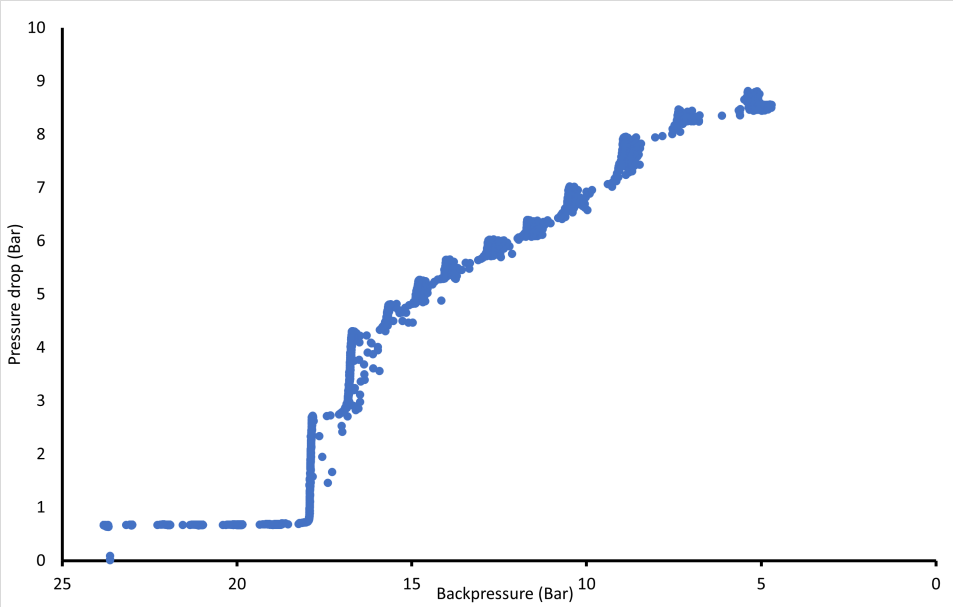

Figure 3.6: Time averaged data of the last interval of the core set out against the pressure

4

Results

In this chapter the results from the various experiments will be shown starting with the results from the single phase water injection experiments, followed by the separate results from the different sets of co-injection degassing experiments.

4.1. permeability tests

Bentheimer sandstone.
Figure 4.1 shows how the pressure drop over the core against the flow rate. As explained before in the procedure section, the permeability was calculated using the Darcy's law and the measured pressure drop as shown in table 4.1.The average permeability for the Bentheimer sandstone core obtained from the three experiments is 2.29 Darcy. The flow rates used are the flow rates at which a transition from laminar to turbulent flow could occur depending on the Reynolds number used. At high flow rates there is still a linear relation between the low rate and pressure drop, this means that the fluid flow is still in laminar flow.

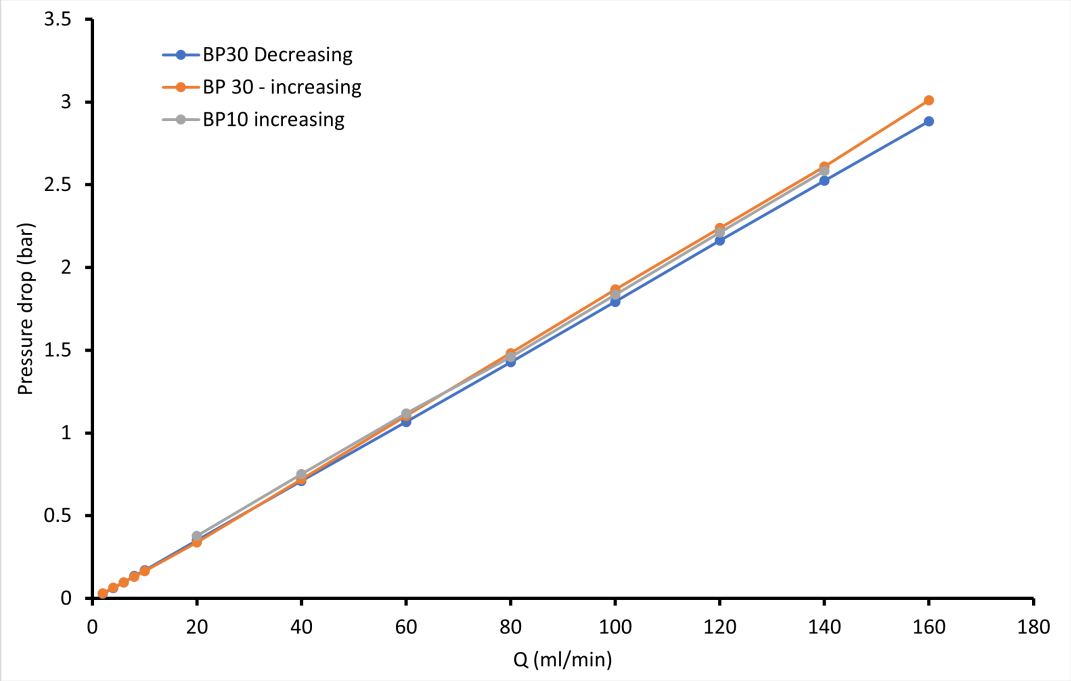

Figure 4.1: Pressure drop measured during single phase water injection experiments set out against flow rate (Q)

Table 4.1: Permeability values measured during single phase water injection experiments and average permeability measured of the Bentheimer sandstone core

Experiment	Permeability (Darcy)
BP30 decreasing flow rate	2.34
BP30 increasing flow rate	2.26
BP10 increasing flow rate	2.27
Average	**2.29**

Berea sandstone.
Figure 4.2 shows that the measured pressure drop at different flow rates is very similar for the two single phase water injection experiments. The measured permeabilities from the two tests, as can be seen in table 4.2, are very similar as well. The average permeability measured for the Berea sandstone core is 0.144 Darcy. The flow rate in the experiment performed at a back pressure of 20 bar was first increased from 0 to 25 mL/min and then decreased again to 15 mL/min to check if this would influence the result.

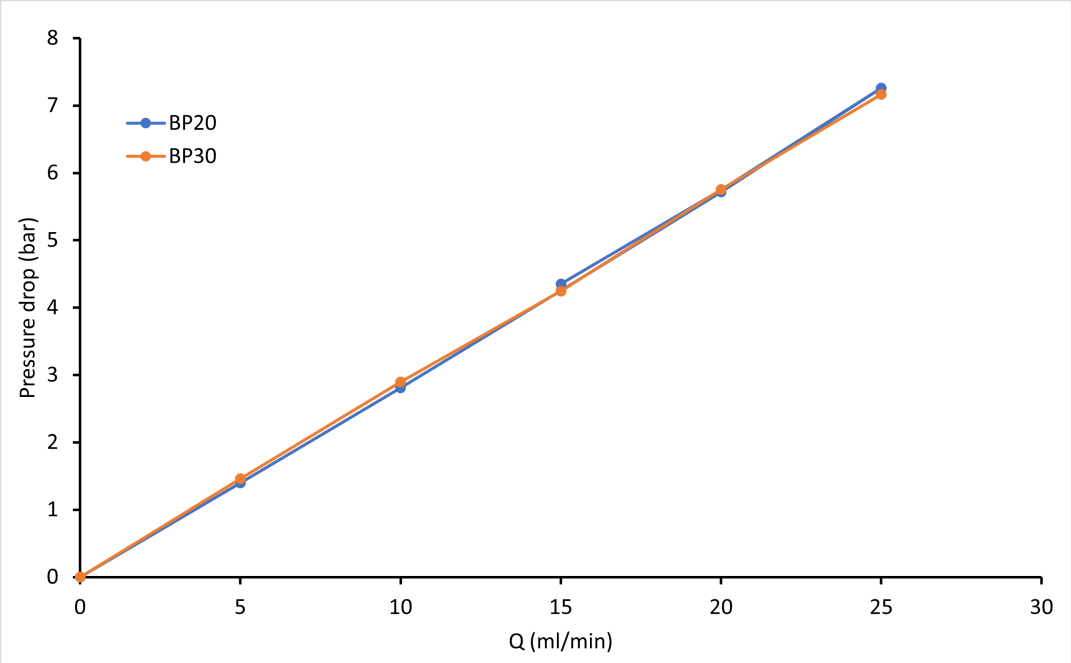

Figure 4.2: Pressure drop measured during single phase water injection experiments set out against flow rate (Q)

Table 4.2: Permeability values measured during single phase water injection experiments and average permeability measured of the Berea sandstone core

Experiment	Permeability (Darcy)
BP30	0.146
BP20	0.143
Average	**0.144**

4.2. Results co-injection degassing experiments

Six sets of experiments were performed to determine at which pressure and gas concentration gas starts to exsolve from solution and to examine what the effect is on the effective permeability at different conditions. The results of these sets are displayed in this section.

4.2.1. Set1: Co-injection of CO_2 and tap water with increasing CO_2 concentrations

In figure 4.3 the pressure drop over the different intervals of the core can be seen for a single experiment that is part of the first set. As can be seen in figure 4.3 the pressure drop over the interval between the 2nd and 3th pressure transducers (at the inlet of the core) increases before the rest of the intervals. Since normally the pressure drop would increase first in the last interval (7-8), this implies insufficient mixing of CO_2 and water before entering the core. Moreover in the last (7-8) and second to last (6-7) interval there is a steady increase in pressure drop from approximately 0.15 to 0.6 when increasing the the CO_2 concentration.

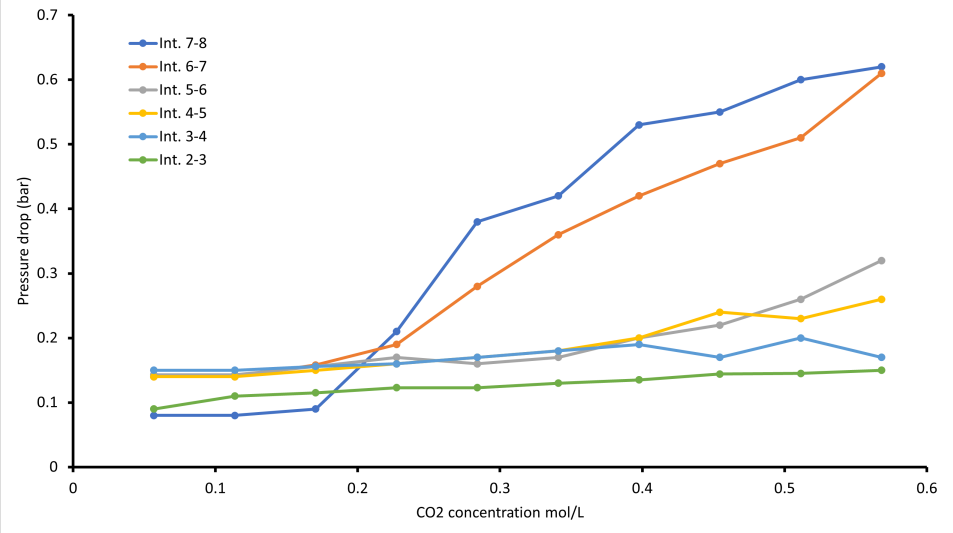

Figure 4.3: Pressure drop over different intervals of the core of a single experiment part of set 1, with 2-3 being the pressure drop over the first interval closest to the inlet, and 7-8 being the pressure drop over the interval closest to the outlet of the core.

Figure 4.4 displays the pressure drop over the last interval of the core for all experiments of the first set, each line shows the results of one experiment that is part of the first set. The experiments were performed at a different pressure set at the backpressure. At low CO_2 concentrations the line is horizontal for all experiments. The pressure drop when the line is horizontal is the initial pressure drop over the last interval of the core before degassing occurs. There difference in the initial pressure drop between experiments, this is due to different flow rates that were used in experiments, that range between 30 and 60 mL/min. At high flow rates the fluid and CO_2 had less time to mix and therefore had a higher chance of not mixing well before entering the core. At low flow rates the mixing was better, but this had the downside of having a lower pressure drop which gives less clear results on the degassing process.

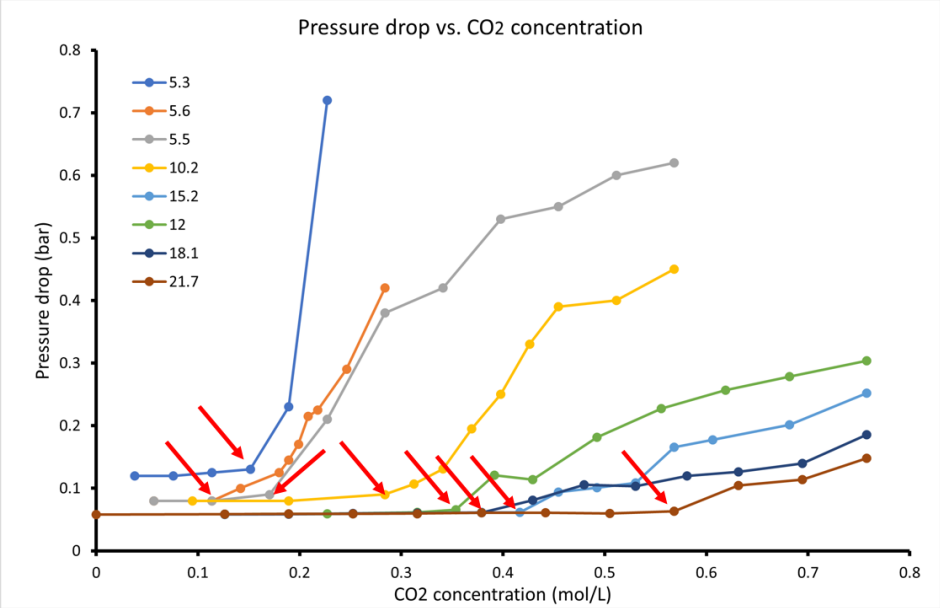

Figure 4.4: Pressure drop over the last interval of the core set out against CO_2 concentration for experiments performed at a different backpressure displayed in the legend. The red arrows indicate the point at which the pressure drop starts to increase and the degassing process starts

During an experiment the CO_2 concentration is increased step wise. At a certain concentration the pressure drop over the last interval of the core increases. This is the point in which the pressure drop starts to deviate from the single phase pressure drop and is assumed to be the moment at which degassing starts (red arrows in figure 4.4). In figure 4.5 the CO_2 concentration at which the degassing process starts are plotted against the backpressure pressure which was set for that experiment. The blue line in figure 4.5 is the maximum CO_2 solubility according to Henry's law, as described in section 2.4 of the theoretical background. The points of onset of the degassing process in the experiments coincides with the maximum solubility of CO_2 according to Henry's law.

Figure 4.5: Onset degassing process of the experiments (red dots) versus Henry's law (blue line)

Using equation 2.4 the effect of degassing on the effective permeability can be calculated using the pressure drop. Figure 4.6 shows how the effective permeability changes with increasing carbon dioxide concentration for experiments performed at a different backpressure. The effective permeability

in each experiment starts out at about 2.3 Darcy in each experiment which is similar to the permeability found in the single phase water injection experiments. When the degassing process starts the effective permeability decreases rapidly and gradually. The effective permeability decreases by one order of magnitude to somewhere in between 0.3 and 0.9 Darcy.

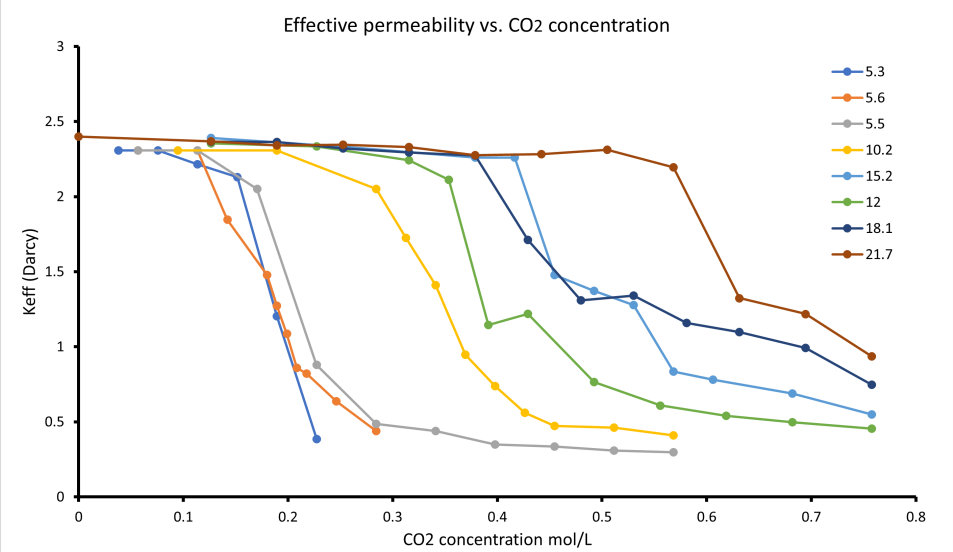

Figure 4.6: effective permeability set out against CO_2 concentration in mol/L for experiments performed at a different backpressure

4.2.2. Set2: Co-injection with a constant CO_2 concentration and flow rate and decreasing backpressure using a Bentheimer core

In figure 4.7 the pressure drop over last interval of the core is plotted against the backpressure for experiments with different CO_2 concentrations. Due to different flow rates at which the experiments were performed the initial pressure drop as well as the maximum pressure drop obtained in the experiments differ from each other. The section of the experiments with a low initial pressure drop were performed at a flow rate of 5 mL/min, while the section with the higher initial pressure drop were performed with flow rates between 15 and mL/min. The low flow rates were initially used because with low flow rates the CO_2 and water mix well, the low flow rates however also resulted in low pressure drops which made it difficult to distinguish what was happening between the different intervals on the core. For more clear results the flow rates were increased.

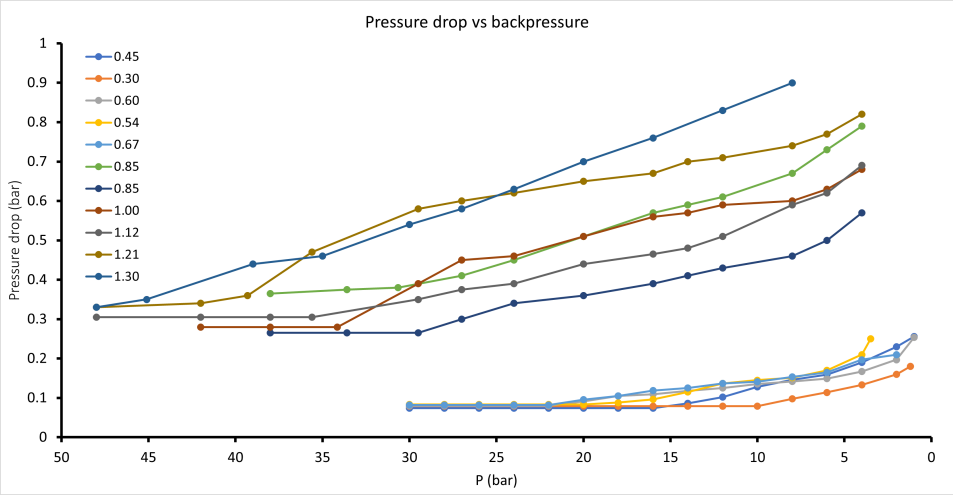

Figure 4.7: Pressure drop over the last interval of the core plotted against backpressure for experiments performed with different CO_2 concentrations displayed in the legend in mol/L

The point at which the pressure drop increases over the interval is assumed to be the moment at which degassing starts. These point are laid out in figure 4.8 together with Henry's law. Similar to the first set, the points of the onset of the degassing process in the experiments coincides to the maximum solubility according to Henry's law for both the experiments performed with high and low flow rates.

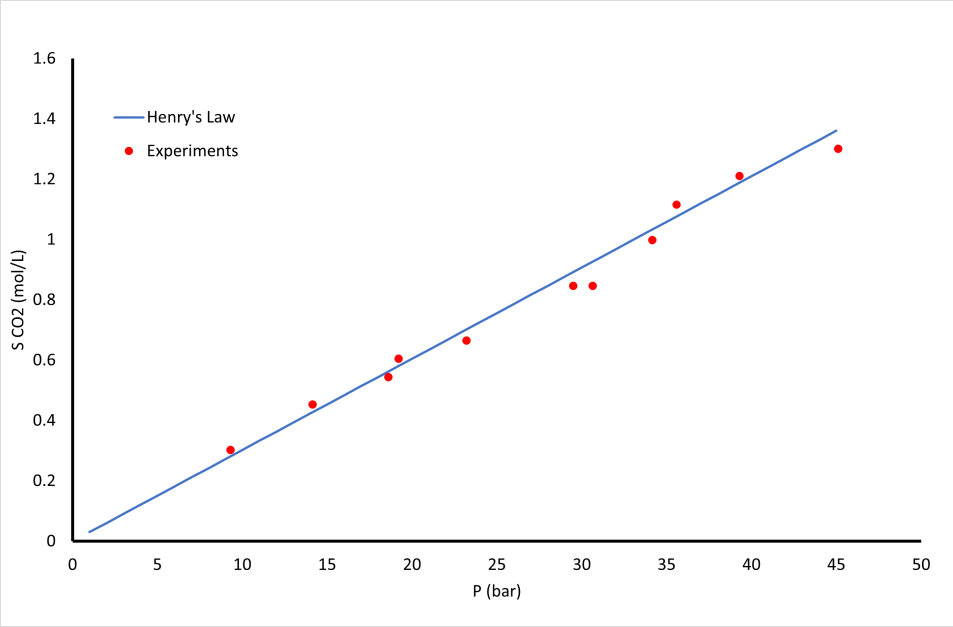

Figure 4.8: Onset pressure degassing process found in experiments (red dots) and Henry's law (blue line)

Using equation 2.4 the effect of degassing on the effective permeability can be calculated using the pressure drop as can be seen in figure 4.9. At the beginning of the experiments, before the degassing process has started, the effective permeability in each experiment is about 2.3 Darcy which is similar to the permeability measured in the permeability test. After the degassing process has started the effective permeability drops gradually in each experiment by one order of magnitude to somewhere in between 1 and 0.6 Darcy.

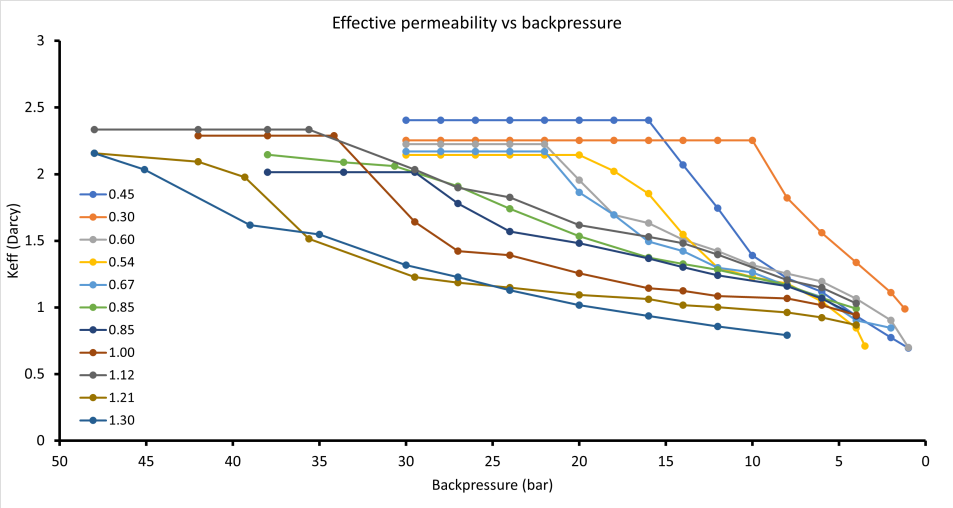

Figure 4.9: effective permeability set out against backpressure for experiments performed with different CO_2 concentrations displayed in the legend

4.2.3. Set 3: Co-injection with a constant CO_2 concentration and flow rate and decreasing backpressure using a Berea core

Figure 4.10 shows the pressure drop over the last interval of the core plotted against the backpressure for experiments with different CO_2 concentrations.

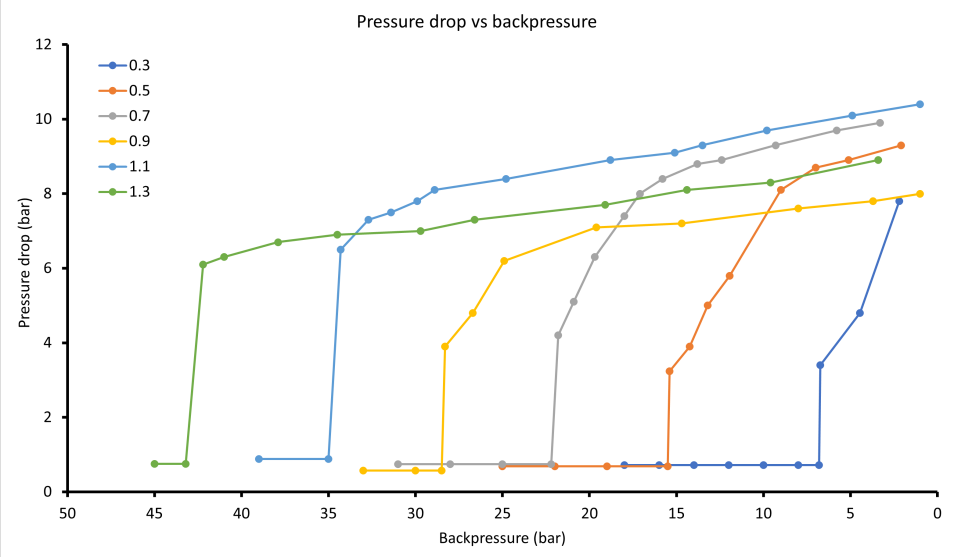

Figure 4.10: Pressure drop set out against backpressure for experiments performed with different CO_2 concentrations displayed in the legend in mol/L

The point at which the pressure drop increases over the interval is assumed to be the moment at which degassing starts. These points are laid out in figure 4.11 together with Henry's law. Similar to the first two sets, the points of the onset of the degassing process in the experiments coincides with the maximum solubility according to Henry's law.

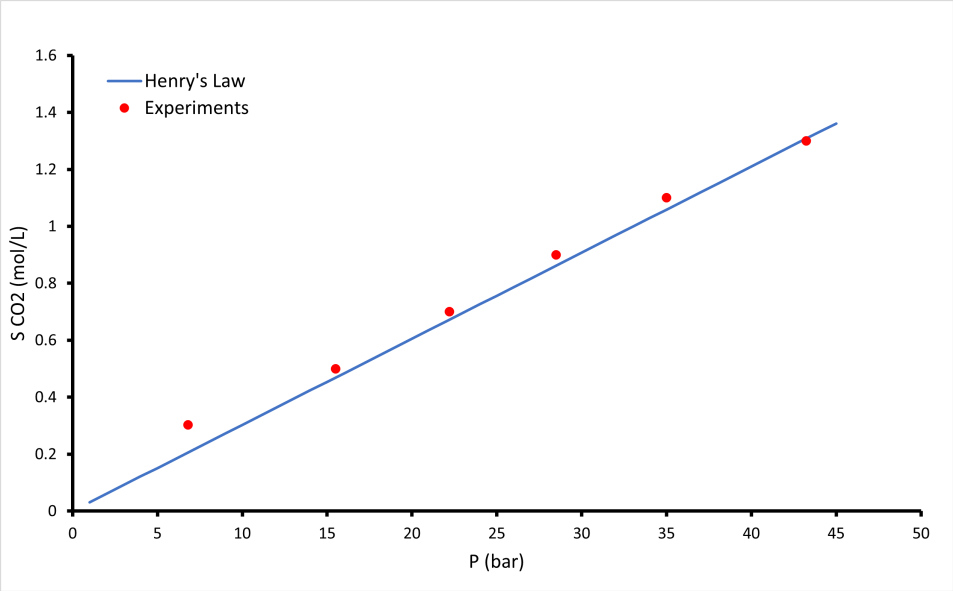

Figure 4.11: Onset pressure degassing process found in experiments (red dots) and Henry's law (blue line)

The effective permeability can be calculated using equation 2.4 and the pressure drop, as can be seen in figure 4.12. Before the degassing starts the effective permeability is about 0.11 Darcy. This value decreases rapidly and instantly when the degassing process starts to about 0.01 Darcy, which is more than a tenfold decrease.

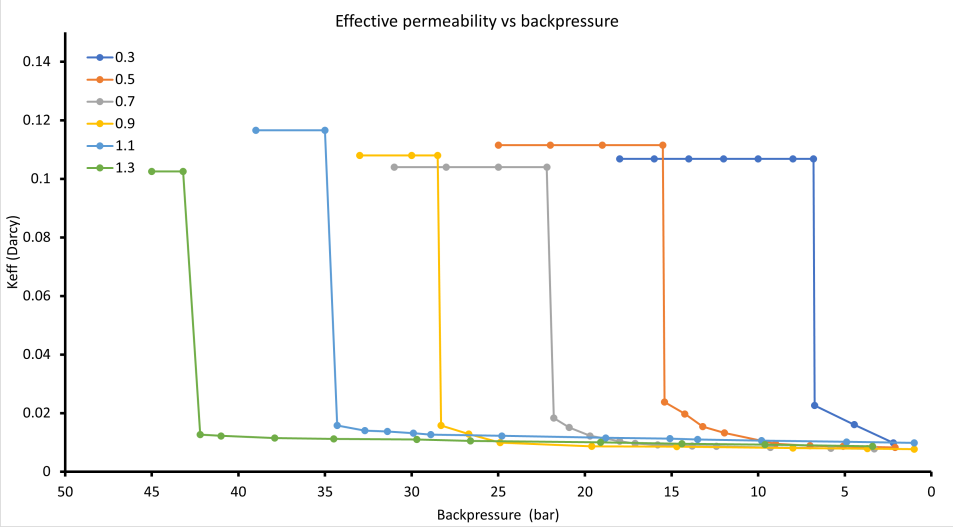

Figure 4.12: effective permeability set out against backpressure for experiments performed with different CO_2 concentrations in mol/L displayed in the legend

4.2.4. Set 4 :Co-injection with a fixed concentration at different temperatures using a Berea core

Figures 4.13 and 4.14 show the pressure drop over the last interval plotted against the backpressure for experiments at a fixed concentration of 0.4 mol/L and 0.2 mol/L respectively. Due to the decreasing viscosity with temperature, the initial pressure drop and the overall pressure drops are lower with increasing temperature. Table 2.5 shows the viscosity values of water at different temperatures.

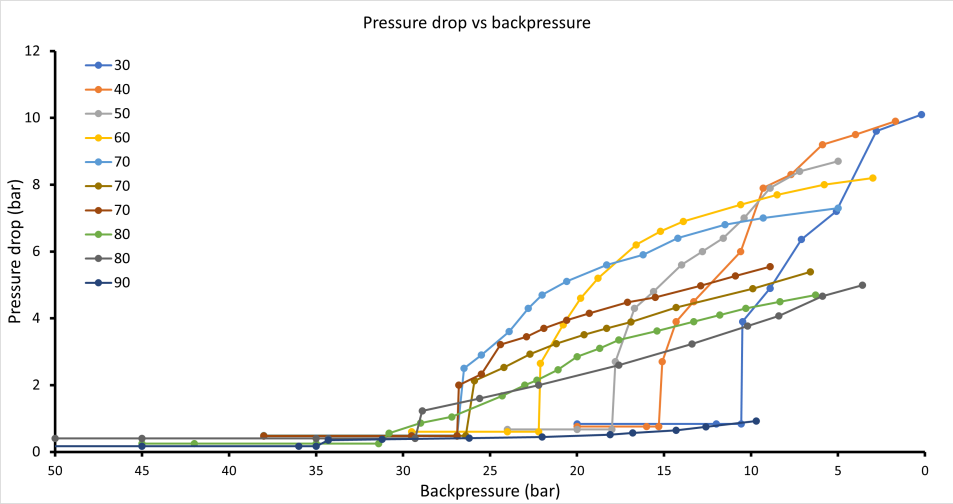

Figure 4.13: Pressure drop set out against backpressure for experiments performed at a constant CO_2 concentration of 0.4 mol/L at different temperatures (°C) displayed in the legend

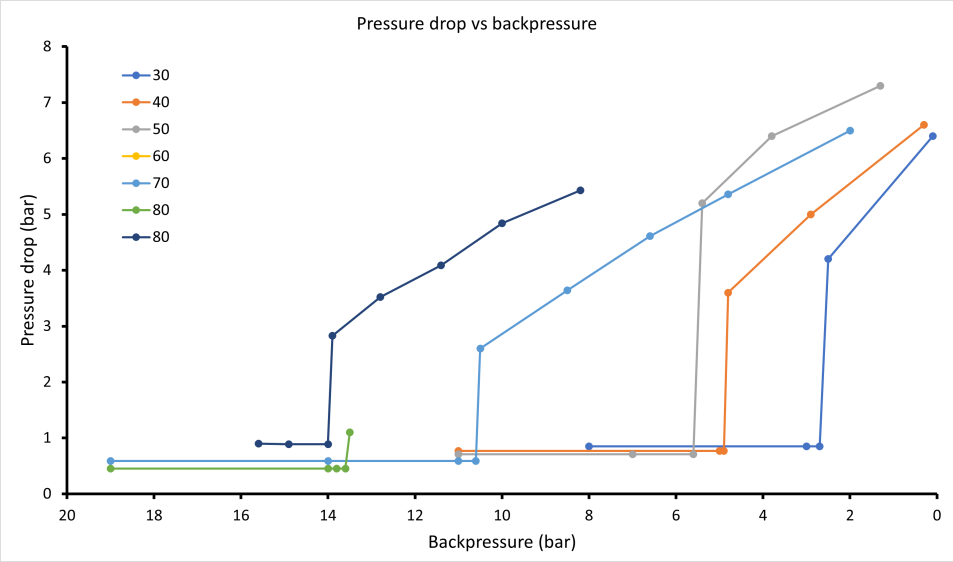

Figure 4.14: Pressure drop set out against backpressure for experiments performed at a constant CO_2 concentration of 0.2 mol/L at different temperatures (°C) displayed in the legend

The point at which the pressure drop increases over the interval is assumed to be the moment at which degassing starts. These point are shown in figure 4.15 for both experiments together with Henry's law that has been modified using the Van 't Hoff equation as discussed in the theory section 2.4 to give the CO_2 solubility at different temperatures for concentrations of 0.4 and 0.2 mol/L.

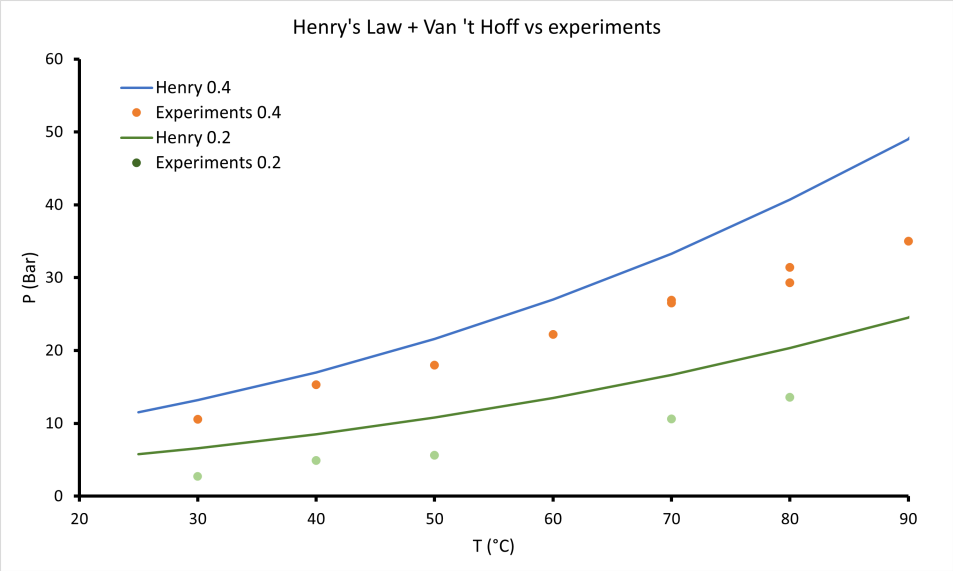

Figure 4.15: Onset degassing process of the experiments with fixed CO_2 concentration of 0.4 mol/L (orange dots) a fixed concentration of 0.2 mol/L (green dots) versus Henry's law for a 0.4 mol/L concentration (blue line) and for a 0.2 mol/L concentration (green line)

With increasing temperatures the conditions at which the degassing process starts to deviate further from Henry's law. This is the case both for the experiments done with a constant CO_2 concentration of 0.2 mol/L and 0.4 mol/L.

Figure 4.16 shows the effective permeability of the experiments calculated using equation 2.4 and the pressure drop. For the experiments performed with a constant carbon dioxide concentration of 0.4 mol/L a distinction can be made between the experiments performed at a temperature up and till 70 °C and at temperatures of 80 °C and higher. At temperatures up and till 70 °C the effective permeability before the degassing process initiates is between 0.1 and 0.08 Darcy. When the degassing process starts the effective permeability drops rapidly to about 0.01 Darcy. The effective permeability of the experiments performed at 80 °C starts between 0.135 and 0.115 Darcy and similarly drop to about 0.01 Darcy. Except the higher initial permeability, the behaviour of these experiments does not seem to deviate from the experiments performed at lower temperatures. At 90 °C the effective permeability starts of a lot higher at about 0.18 Darcy, which is higher than the permeability measured in the single phase water injection experiments. The behaviour of this experiment also differs from the other experiments performed at lower temperatures.

The initial effective permeability's of the experiments of 80 °C and above differ from the experiments at lower temperatures. A possible reason for this is that the combination of high temperatures and the large fluctuation in pressure. At high pressures the PEEK core holder can become slightly ductile together with large fluctuation in pressure this can cause the PEEK core holder and the pressure transducers to not optimally connect with each other. This could result in the initial pressures that are measured at high temperatures to differ from the rest.

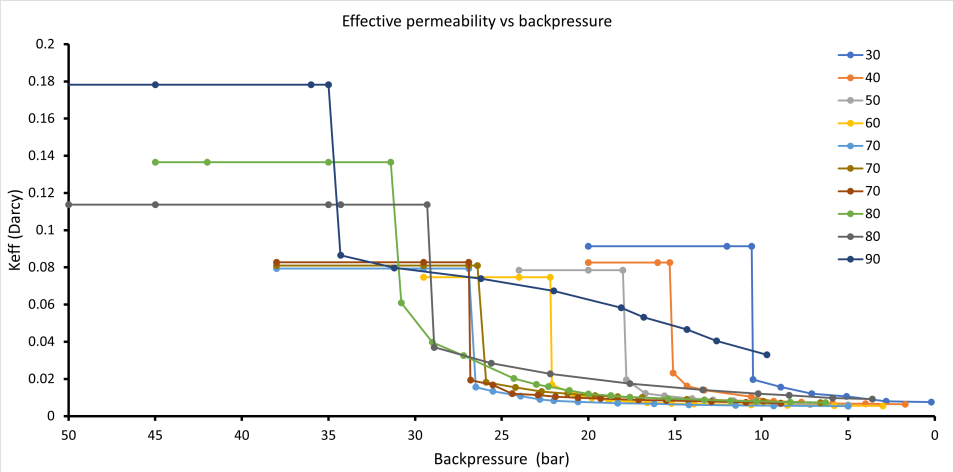

Figure 4.16: effective permeability set out against backpressure for experiments performed at a fixed CO_2 concentration of 0.4 mol/L at different temperatures displayed in the legend

Figure 4.17 shows the effective permeability of the experiments calculated using equation 2.4 and the pressure drop. The effective permeability does not differ much between the experiments, except one of the experiments performed at 80 °C. The deviating experiment was the very last experiment performed of all experiments. The core was extensively flushed to get the remaining CO_2 out but the pressure drop over the last interval remained high. So either there was some blockage in the core or the pressure transducers did not measure correctly. The behaviour of this experiment does not deviate from the others. Also the point at which the degassing process starts is similar to the unfinished 80 °C experiment from which it can be concluded that this lower initial effective permeability does not influence the point at which the degassing starts.

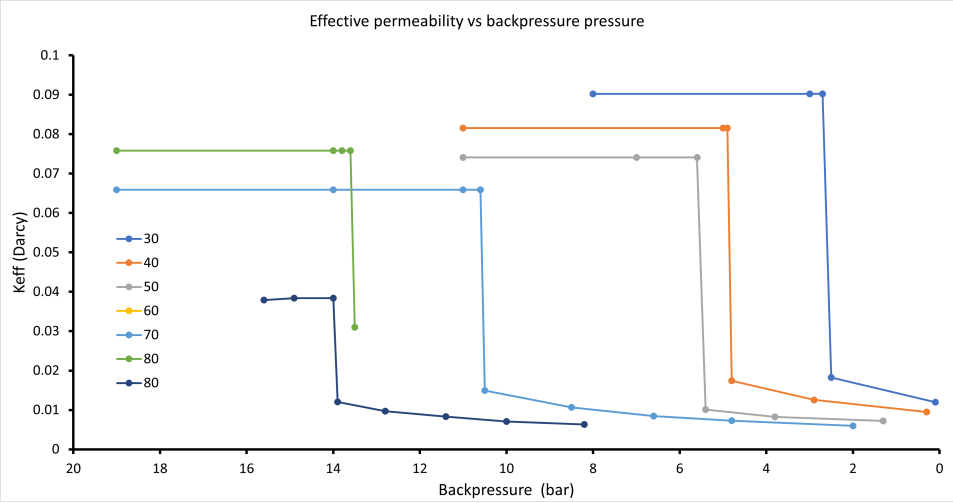

Figure 4.17: effective permeability set out against backpressure for experiments performed at a fixed CO_2 concentration of 0.2 mol/L at different temperatures displayed in the legend

4.2.5. Set 5: Co-injection at 70°C with different CO_2 concentrations

Figure 4.18 displays the pressure drop over the last interval of the core plotted against the backpressure for experiments with different CO2 concentrations. This set of experiments was performed for CO_2 concentrations between 0.2 and 0.9 mol/L.

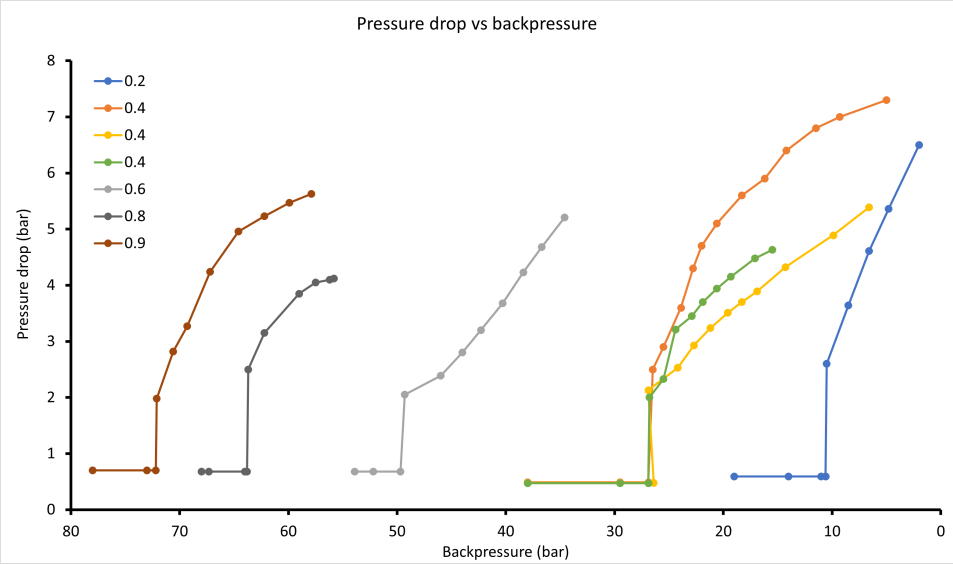

Figure 4.18: Pressure drop plotted against backpressure for experiments performed with different CO_2 concentrations in mol/L displayed in the legend

What can be observed in figure 4.18 is that for the experiments in this set there is a rapid increase in pressure drop once the degassing process has started. This fast increase in pressure drop is similar to what could be seen in the earlier two sets of experiments performed on the Berea core. The point at which the pressure drop increases over the interval is assumed to be the moment at which degassing starts. These point are laid out in figure 4.19 together with Henry's law. What this figure shows is that the points at which the degassing starts in the experiments is systemically at a lower pressure than the maximum solubility according to Henry's law.

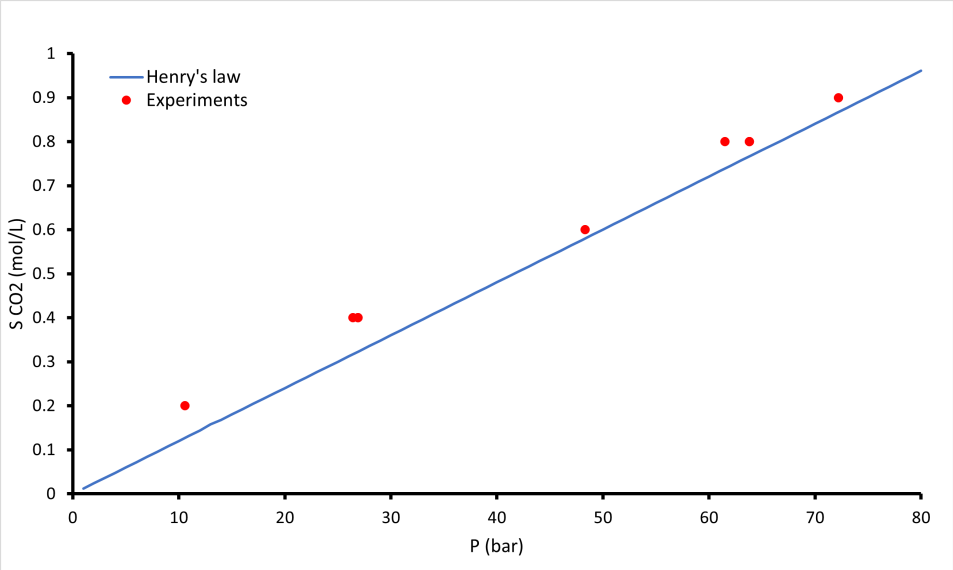

Figure 4.19: Onset degassing process of the experiments (red dots) versus Henry's law (orange line)

The effective permeability can be calculated using equation 2.4 and the pressure drop, as can be seen in figure 4.20. The behaviour of the different experiments in this set is more or less the same. The initial effective permeabilities are between 0.065 and 0.082 Darcy and all drop to below 0.01 Darcy.

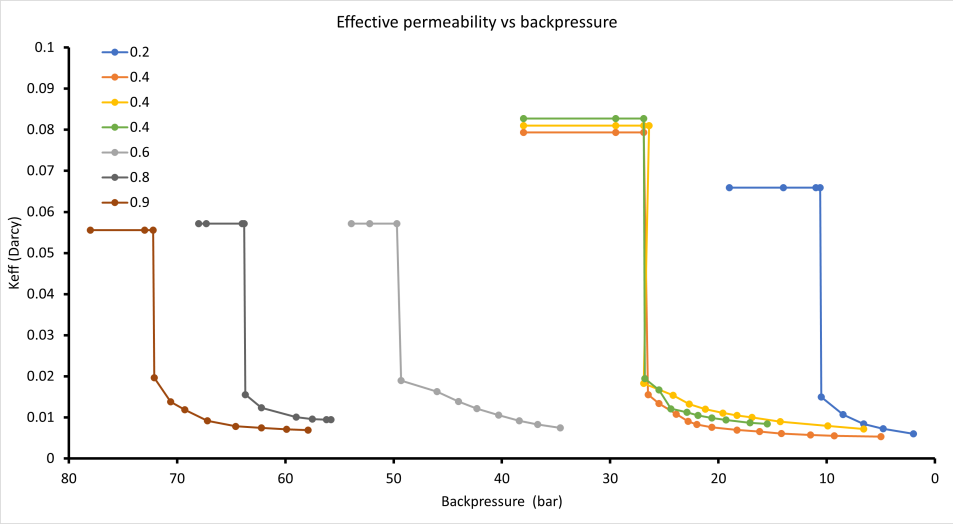

Figure 4.20: effective permeability set out against backpressure for experiments performed with different CO_2 concentrations displayed in the legend

4.2.6. Set 6: Co-injection of CO_2 and a 1M NaCl solution at 70°C with different CO_2 concentrations

Figure 4.21 displays the pressure drop plotted against the backpressure for experiments with different CO_2 concentrations between 0.2 and 0.8 mol/L.

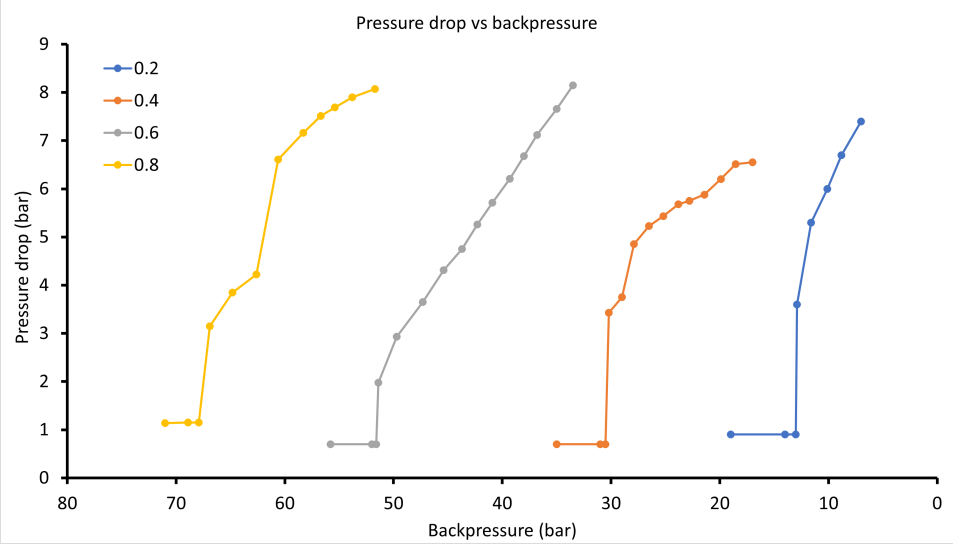

Figure 4.21: Pressure drop set out against backpressure for experiments performed with different CO2 concentrations displayed in the legend

Figure 4.21 shows similar pressure drops for the different experiments performed with different CO_2 concentrations. The initial pressure drop over the last interval of the core starts of at about 1 bar when the degassing process starts the pressure drop increases rapidly in similar fashion. The point at which the pressure drop increases over the interval is assumed to be the moment at which degassing starts. These point are laid out in figure 4.22 together with the maximum solubility of CO_2 at 70°C according to Henry's law. What is good to note here is that Henry's law here is for pure water, while in the experiments a brine solution was used.

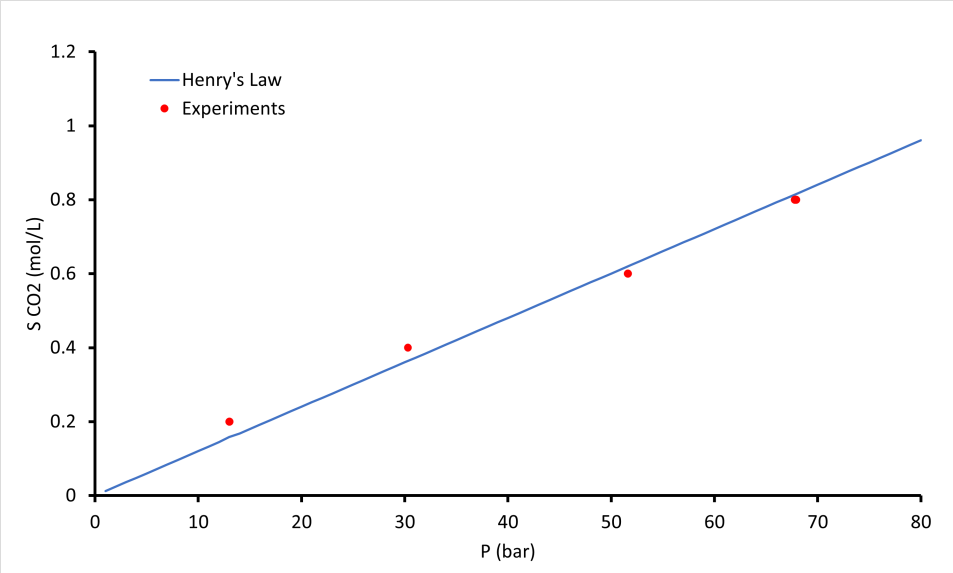

Figure 4.22: Onset degassing process of the experiments (red dots) versus Henry's law (orange line)

Figure 4.23 shows the effective permeability calculated using equation 2.4 and the pressure drop. There is a quite broad range in the initial effective permeability in the experiments, ranging from 0.047 Darcy in the experiment performed with a CO_2 concentration of 0.8 mol/L and 0.085 Darcy in the experiment performed with a CO_2 concentration of 0.6 mol/L. This difference in initial effective permeability does not influence the relative change in effective permeability since they drop 92% and 91% respectively.

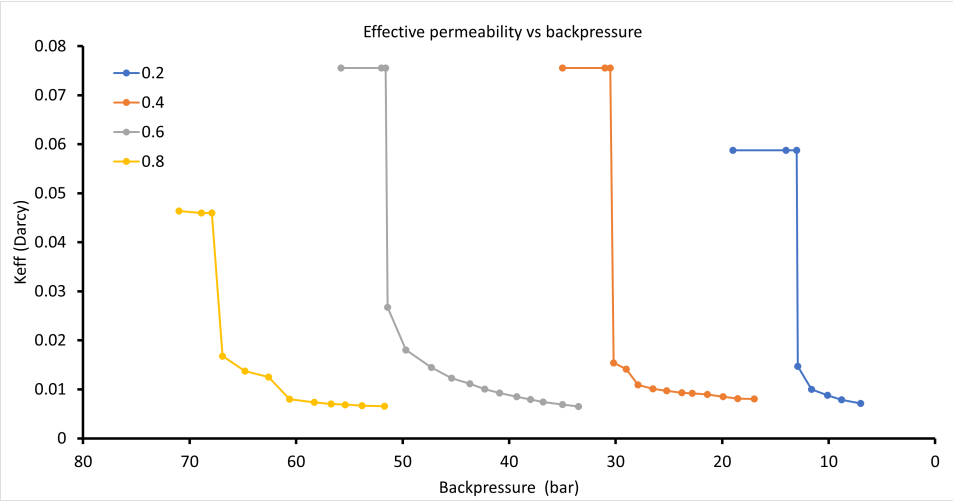

Figure 4.23: effective permeability set out against backpressure for experiments performed with different CO_2 concentrations displayed in the legend

5

Discussion

The aim of this thesis is to find the point at which the degassing process takes place and what the effect of this process is on the effective permeability of a reservoir rock. In this section this will be discussed for different variables that influence the degassing process and the effect on the effective permeability. First the influence of the reservoir rock characteristics will be discussed. Subsequently we will have a look at the influence of the temperature. The third variable that will be discussed is the effect of the salinity of the fluid on the process. Next the reversibility of the degassing process will be discussed. This chapter will conclude itself with the implications of this study.

For the reliability of the data it is important to see what the repeatability of the experiments is. Therefore several experiments were performed multiple times. Table A.1 in appendix A shows the parameters and the dates of all experiments performed. Note that in particular experiment 4.6, 4.13, and 5.1 were performed identically in time span of two months. The onset of the degassing for these three experiments lay between a range of 0.5 bars. Experiment 4.8 and 4.12 were performed identically one week after each other with the onset of degassing differing 2 bars between them. Experiment 4.9 and 4.14 were performed identically with seven weeks in between them with the onset of degassing differing 0.4 bars between them.

5.1. Influence pore scale characteristics reservoir rock

The first three sets of experiments have been performed at the same conditions, namely at 30 degrees Celsius. The method between the first and the latter two does differ and the core that was used differs between the first two and the third set of experiments. In figure 5.1 the onset of the degassing process for the three different sets of experiments in combination with Henry's law shows that for all three experiments the moment at which the degassing process starts coincides well to what can be expected from Henry's law. So at the conditions of 30 degrees Celsius and pressures up to 45 bars, Henry's law gives a good indication for when the degassing process starts. Set 2 and set 3 are performed in the same manner only differing in the core used, set 2 with a Bentheimer sandstone core and set 3 with a Berea sandstone core. Comparing these two sets shows that the conditions at which the degassing process starts is independent of the type of rock and its properties. By comparing the first two sets of experiments it can also be said that the procedure in which the experiments are performed also does not have an influence on conditions at which the degassing process starts, which increases the certainty of the results.

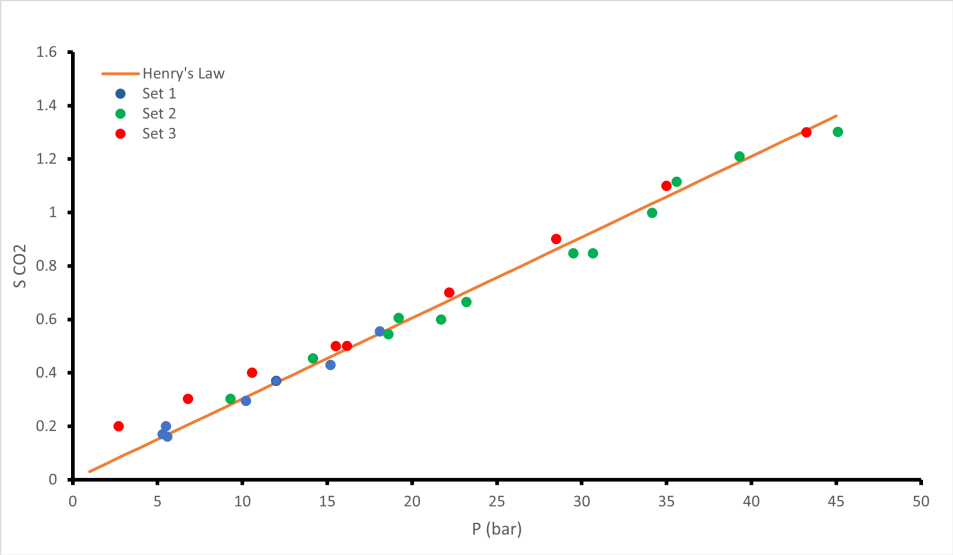

Figure 5.1: The onset of the degassing process of the first three sets experiments (dots) together with Henry's law (orange line), Set 1 and 2 were performed on the Bentheimer sandstone core, Set 3 on Berea sandstone core

Where the two different cores are set apart is the influence of the degassing process on the effective permeability. While the onset of the degassing process is similar for the two cores, the rate at which effective permeability is affected and the extent to which it is affected differs significantly. The Bentheimer and the Berea sandstone have a different initial permeability. Therefore, in order t compare the two rock types I have calculated the average percentual change in effective permeability of the cores after the onset of the degassing process, see figure 5.2. This shows that when the pressure drops 1 bar below the pressure at which the degassing process starts the effective permeability deceases by 11 percent for the Bentheimer, while for the Berea this is on average 82 percent. At 5 bars below the degassing pressure the effective permeability has decreased on average 30 percent for the Bentheimer and 89 percent for the Berea. A further decrease in pressure will not have a significant effect on the effective permeability after this point for the Berea. For the Bentheimer sandstone the effective permeability will on average decrease up till the point that the pressure is 15 bars lower than the onset of the degassing process. At this point the effective permeability will have decreased on average 48%, a further decrease in pressure will not significantly decrease the effective permeability any further.

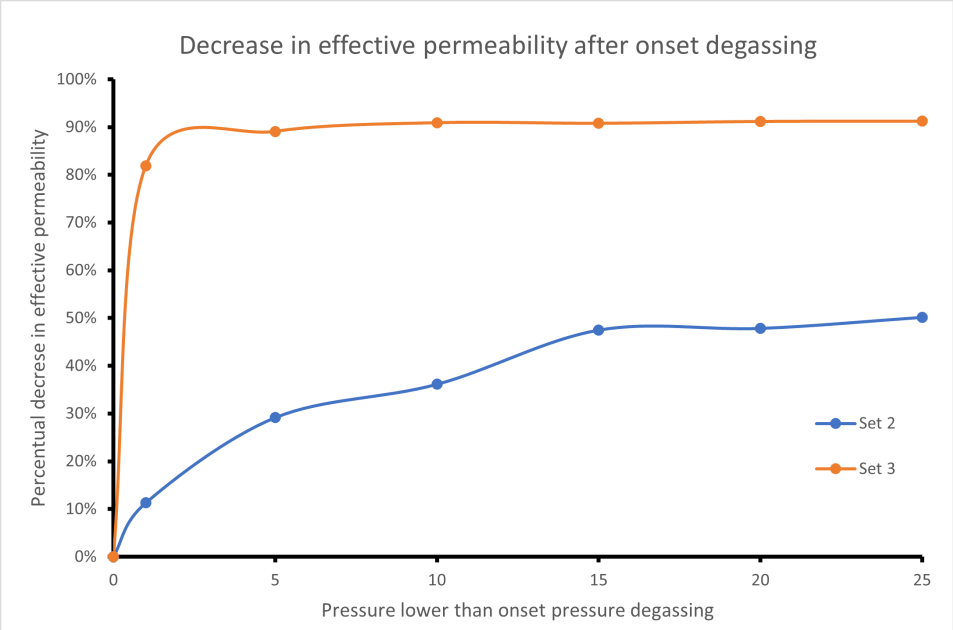

Figure 5.2: This figure shows the reduction in effective permeability (percentage) after the degassing process has started for set 2 (blue line) which was performed on the Bentheimer sandstone core, and for set 3 (orange line) which was performed on the Berea sandstone core

The difference in how the degassing process influences the effective permeability of the different rocks can be linked back to their pore scale characteristics. Bubbles can get stuck in a pore when the bubble radius exceeds the radii of the pore throats connected to that pore (Mahabadi, 2018). Theory subsection 2.6 shows that the pore radii of the Berea sandstone are significantly smaller than the pore radii of the Bentheimer sandstone. This means that smaller bubbles have the potential to clog pores in the Berea could pass through the Bentheimer pores without blocking them. The Berea sandstone pore network is more easily blocked than the Bentheimer sandstone pore system. This causes the degassing process to influence the effective permeability of the Berea by a greater amount than the Bentheimer sandstone.

The rate at which a decrease in pressure beyond the onset of the degassing process influences the effective permeability most likely has the same origin. A bubble can get trapped upon nucleation when the bubble radius at nucleation is larger than the radii of the pore throats connected to the pore space it nucleates in (Mahabadi, 2018). The size of the bubbles among nucleation is most likely large enough to cause blocking of pore space at the Berea sandstone, hence the fast decrease in effective permeability. For the Bentheimer sandstone the bubbles are not big enough at nucleation to cause blockages since the pore radii in the Bentheimer are larger. For the bubbles to block the pore they first have to increase in size, this can happen due to the merging of two bubbles or due to gas expansion caused by a further decrease in pressure.

What also can be noticed is that no matter how much the pressure decreases and how much gas gets exsolved from water there remains a flow of water through the core. The degassing of carbon dioxide from water does not cause a complete block to water. In the Berea sandstone core degassing can results in a effective permeability decrease of about 90% but ultimately this means that 10% remains and water can still flow through the core. For the Bentheimer this permeability reduction is less extreme in which case more than 50% of the effective permeability remains.

In the third set of experiments there was a larger deviation between the maximum solubility according to Henry's law and the experiments at low pressures than at high pressures. Deviations to Henry's law (Chang & Thoman, 2014, p. 226) can occur if the dissolved gas interacts chemically with the solvent. CO_2 react with water due to which it has a high solubility. When CO_2 dissolves into water it reacts to carbonic acid (H_2CO_3). Depending on the acidity of the solution the carbonic acid can react further

and lose one or two more protons. For the CO_2 to exsolve from solution as a gas the reactions first have to reverse to form CO_2 in solution. The driving force for these reactions in the experiments is the pressure, where a decrease in pressure will push the equilibrium in the direction with more molecules (Chang & Thoman, 2014, p. 326). At low pressures this driving force to push these reactions is smaller which might cause the deviations from Henry's law to be larger than at high pressures where there is a larger driving force.

5.2. Influence temperature on degassing process

The degassing process is not only influenced by the pore scale characteristics. As discussed in the theoretical background the temperature also has a significant impact. When the temperature increases less gas can be dissolved in water. This means that for a constant CO_2 concentration the degassing process occurs at a higher pressure with increasing temperature. In set 4 experiments were performed to find the onset of the degassing process and its effect on the effective permeability for two CO_2 concentrations at different temperatures. Figure 4.15 shows the onset of the degassing process in these experiments together with the maximum amount of CO_2 that can be dissolved according to Henry's law using the Van 't Hoff equation to correct it for elevated temperatures. As discussed in the results, the conditions at which the degassing process starts seems to deviate further from the maximum CO_2 concentration that can be dissolved at a given pressure according to Henry's law with increasing temperature for both CO_2 concentrations of 0.2 mol/L and 0.4 mol/L.

A possible explanation for the increasing difference between Henry's law and what is found in the experiments can be found in extrapolation process used to adapt Henry's law for other temperatures than for which the values are known at 30°C. The values for Henry's at different temperatures were extrapolated from a single known value for Henry's constant using the Van t' Hoff equation which uses the enthalpy of solution (equation 5.1) (Sander, 2015). The experiments performed at the lower end of the temperature range researched, and therefore closer to the temperature from which the values were extrapolated from, coincide closer to the maximum dissolved CO_2 concentrations according to Henry's law. As the temperature increases, and moves further from the temperature from which the values were extrapolated from, the values obtained from the experiments coincide less with Henry's law.

$$H(T) = H^{\circ} \exp\left[\frac{-\Delta_{sol} H}{R}\left(\frac{1}{T} - \frac{1}{T^{\circ}}\right)\right] \tag{5.1}$$

H(T) is the Henry's law constant at the required temperature T, H^0 is Henry's law constant at reference temperature T^0 of 298.15 K, $\Delta_{sol} H$ is the enthalpy of dissolution that is independent of temperature (Sander, 2015). The enthalpy of dissolution value used in the results and in figure 4.15 is 2400 (J/PV).

The enthalpy of dissolution of CO_2 value that should be used is not undisputed. Sander (2015) has conducted an extensive literature review for these values. More than half of the authors (11/21) agree on a enthalpy of dissolution value of 2400 (J/PV) for this, the other values vary between 2200 and 2900 (J/PV). Figure 5.3 shows Henry's law extrapolated for different temperatures using the Van t' Hoff equation for different enthalpy of dissolution values.

The difference in the enthalpy of dissolution values most likely originates from the method used to obtain them. The highest value of 2900 (J/PV) comes from an article of Kühne et al. (2015) in which a model was created based on the chemical structure of the compounds. The lowest value of 2200 (J/PV) comes from Zheng et al. (1997) in which a degassing system was used to obtain solubility data at different temperatures for low pressures. Extrapolating Henry's law using the lower enthalpy of dissolution value gives a maximum CO_2 solubility estimate that coincides closer to the data obtained from the experiments. The method used to obtain this lower value also is a closer match to this research since it also looked at degassing.

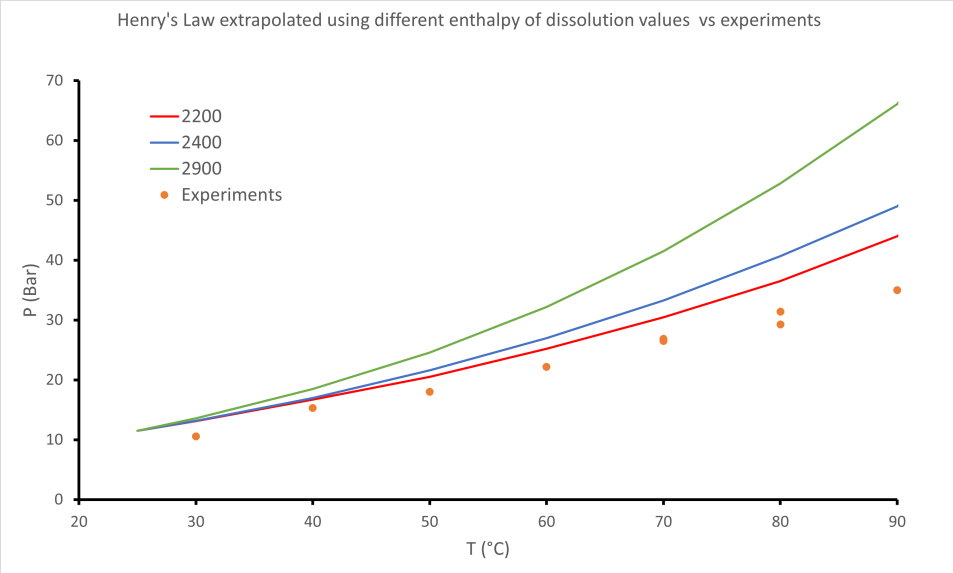

Figure 5.3: This figure shows the Henry's law for a CO_2 of 0.4 mol/L extrapolated for different temperatures using the Van 't Hoff method for different enthalpy of dissolution values together with the points at which the degassing process starts in the experiments

A second possible possible explanation could be that the fluid that is being injected into the core did not heat up all the way to the temperature to which the oven is set. There is a iron spiral in the oven of 2 meters length with the aim to heat the fluid before it enters the core. It could be the case that the time spent in the spiral was not sufficient to heat the it to the required temperature. In this case the points measured in the experiments is actually closer to Henry's law than thought before.

In order to try and test what the extend of this problem heated tap water at a know temperature was injected in the core while the oven was at the same temperature. The temperature of the fluid was again measured at the point were it got disposed in the sink. At this point the fluid already passed the backpressure and about two meters of tubing in which it cooled down. This was done for two temperatures of 40°C and 60°C. Fluid injected at 60°C in a 60°C oven exited the system at a temperature of 38°C, while non-heated tap water injected in a 60°C exited the system at 35°C. Fluid injected at 40°C in a 40°C oven exited the system at a temperature of 27°C, while non-heated tap water injected in a 40°C exited the system at 26°C. What this shows is that the non-heated tap water did not heat all the way to the oven temperature. Since it was only possible to measure the temperature after the fluid exits the system where it had already cooled down substantially, it is difficult to say how much the temperature of the fluid differs from the temperature in the oven. The difference between the fluid temperature and the oven temperature seems to increase with increasing oven temperature. This would result in an increasing error with temperature in which the points measured in the experiments would actually be closer to Henry's law. By measuring the temperature in the sink it can be concluded that the error in temperature is at least 2°C but this error is most likely more in the direction of 5°C.

The third and the fifth set of experiments were performed in the same way on the same core sample, with the only difference between the two sets being the temperature of the oven. The third set was performed at a temperature of 30°C while the fifth set was performed at a temperature of 70°C. Comparing these two sets demonstrates the influence of temperature on the change in effective permeability due to degassing. Figure 5.4 shows the decrease in effective permeability after the degassing process has started. What this figure shows is that at the 30°C the effective permeability drops faster than at 70°C. For the experiments performed at 30°C the effective permeability decreases 88% in about half a bar from which it does not decrease much further, to 91% at 10 bar below degassing pressure. For the experiments performed at 70°C the effective permeability decreases 77% when the degassing process starts. In these experiments however there is a further decrease in effective permeability to 89% at 10 bars below the degassing pressure.

The difference in this behaviour is most likely due to their difference in viscosity. The viscosity of water at 30°C is significantly lower than at 70°C, which are 0.8007 mPa*s and 0.4127 mPa*s respectively. As discussed in section 2.5, the CO_2/water inter facial tension decreases slowly decreases with temperature and therefore causes the capillary pressure to also decrease with temperature. With increasing temperature the capillary forces that trap bubbles in pores decreases. This may cause bubbles to escape from pores at 70°C that would have been trapped at 30°C.

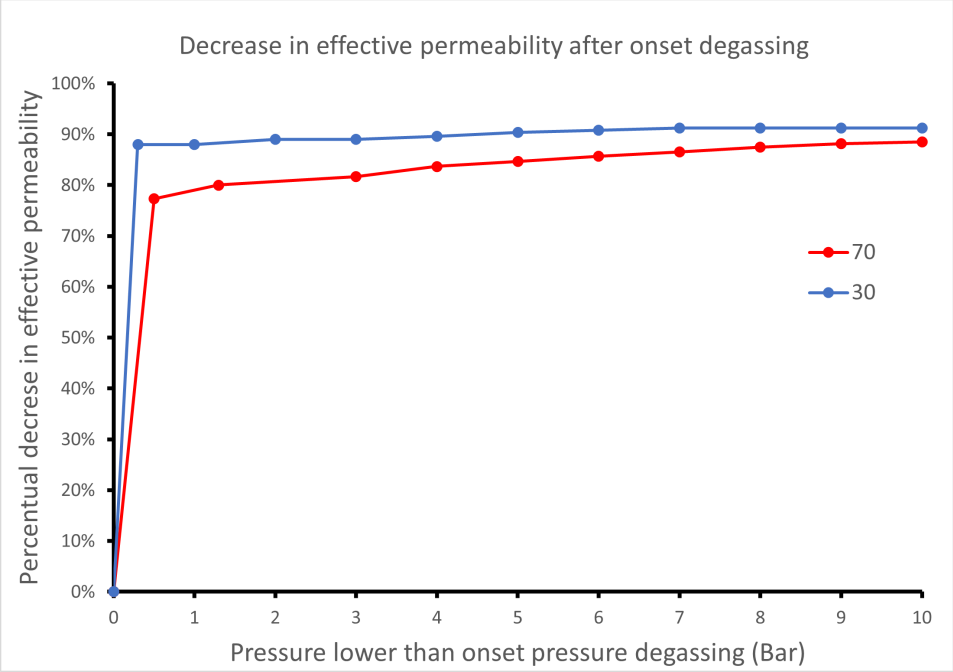

Figure 5.4: This figure shows the average reduction in effective permeability (percentage) after the degassing process has started for experiments performed at temperatures of 30°C and 70°C

5.3. Influence salinity on degassing process

A third factor that influences the degassing process is the salinity of the solution in which the CO_2 is dissolved. As discussed in the section 2.3, with increasing dissolved solids less CO_2 can be dissolved. Set 5 and 6 were performed were performed in the same manner under the same conditions, with the only difference being that the sixth set was performed with a 1M NaCl solution and the fifth set with tap water. Due to the salinity of the brine the viscosity changes from 0.4127 mPa*s for tap water to 0.48 mPa*s for brine (Sharaqwy et al., 2010). The onset of the degassing process in these two sets of experiments can be seen in figure 5.5. What this figure shows is that the degassing process starts at a higher pressure when a brine solution is used instead of tap water. This is not a surprise, since, as discussed earlier in the theory, less gas can be dissolved in saline solutions than in pure water. This causes the degassing process to start at a higher pressure.

The onset of the degassing process of the degassing process for the experiments performed using a brine solution appear to coincide closely with the maximum solubility of CO_2 using Henry's law extrapolated for a temperature of 70°C using the Van 't Hoff equation. As discussed in the last section on the influence of temperature on the degassing process, at high temperatures the extrapolated Henry's law does not give a good indication for the onset of the degassing process for pure water, as the pressure at which the degassing starts in the experiment is significantly lower. The increase in pressure at which the degassing process starts due to the salinity of the solution cancels out the the lower onset pressures measured in the experiments. The appearance that brine solution does coincide well with the extrapolated Henry's law is coincidental.

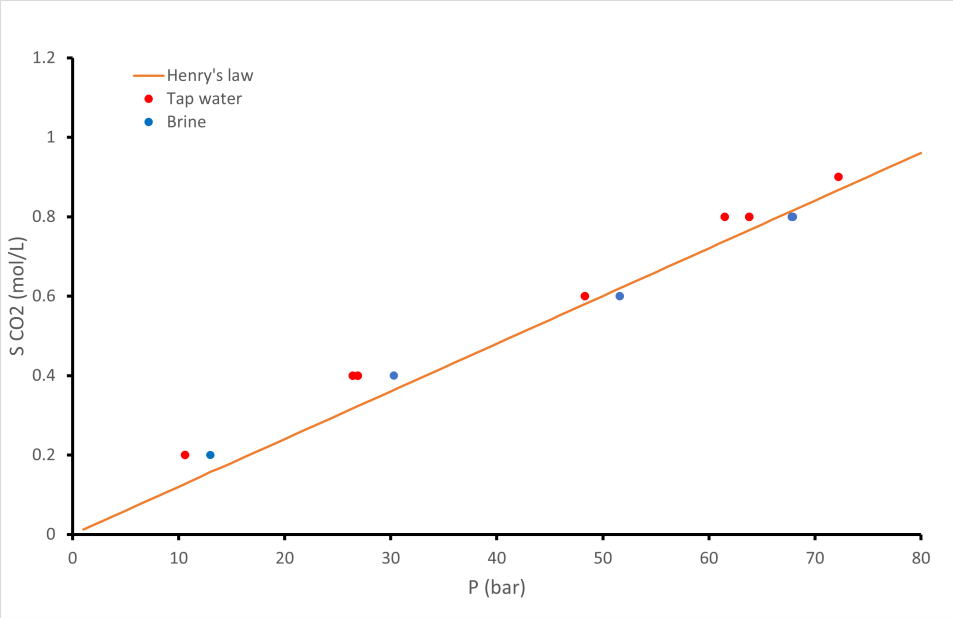

Figure 5.5: Onset degassing process of experiments performed with tap water (red dots) and with a brine solution (blue dots) together with the maximum CO_2 concentration according to Henry's law for pure water

The change in effective permeability between the experiments performed with brine and tap water can be seen in figure 5.6. The behaviour of the experiments performed with brine does not seem to be different than the ones performed with tap water. Salinities in water slightly increases the inter facial tension (IFT) of water (section 2.5). In a brine solution the capillary forces responsible for trapping bubbles should therefore be larger than in tap water. The change in effective permeability in the experiments performed with brine and tap water do not show this. It might be the case that the salinity of the brine solution is not high enough to really cause a change in IFT. The article of Chiquet et al. (2007) stated that in low salinity NaCl (20g/L) solutions there was no noticeable effect of salinity on the IFT. High salinities (3-5 M NaCl) however should increase the IFT slightly. The brine used in the experiment was a 1 M (58 g/L) NaCl solution, which is closer to the low salinity discussed in the article than the high salinity discussed. Therefore the change in IFT due to the salinity might be negligible in this case and not cause real change between the brine and tap water.

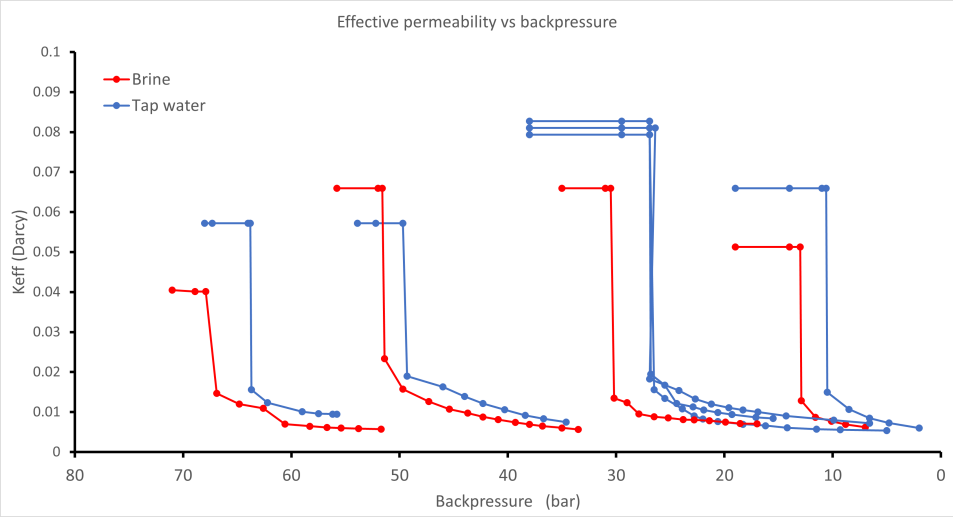

Figure 5.6: effective permeability of individual experiments performed with tap water (blue lines) and with a brine solution (red lines)

5.4. Reversibility of the degassing process

To check the reversibility of the degassing process an experiment was performed like by decreasing the backpressure and at the point where the experiment normally would be finished the backpressure was slowly increased to the pressure the experiment started with. Figure 5.7 shows how the effective permeability changes first by decreasing the backpressure and later by increasing the backpressure. What this shows is that the effect of degassing on the effective permeability can be reversed by increasing the pressure. The pressure at which the effective permeability is restored to its initial value is however higher than the pressure at which the degassing process starts.

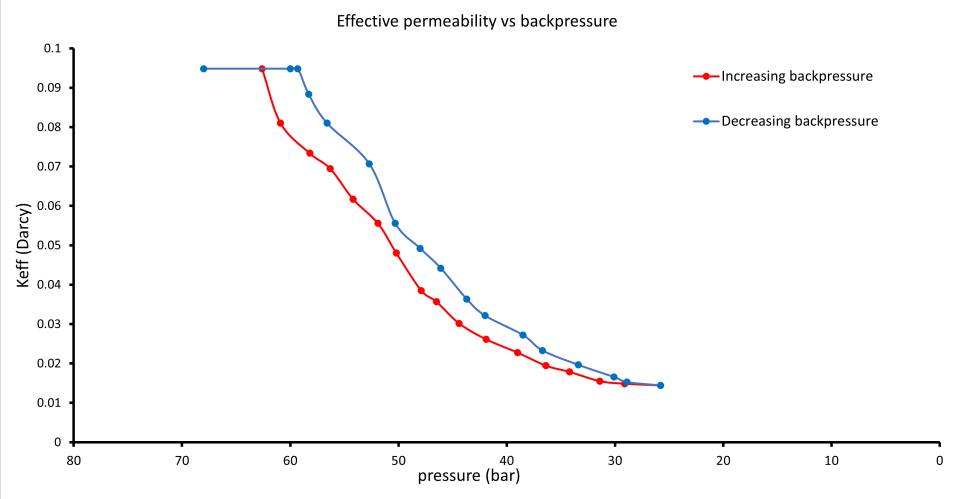

Figure 5.7: Change in effective permeability of a single experiments due to decreasing the backpressure (blue line) and later increasing the backpressure (red line)

Henry's law works both ways, by lowering the pressure during an experiment CO_2 comes out of solution because the at a certain pressure the CO_2 concentration becomes to high for that pressure. But when the pressure increases more CO_2 can be dissolved decreasing the amount of free gas and increasing the effective permeability.

The pressure at onset of the degassing process and the pressure at which the effective permeability has returned to its initial value differ from each other. This is possibly due to just above the degassing pressure there is no CO_2 being released from solution, but it can also not dissolve more CO_2. For the remaining CO_2 bubbles to get dissolved into the fluid the pressure has to increase further.

5.5. Recommendations

For further research into the degassing process with coreflood experiments the following are the recommendations.

- One of the causes of errors in the experiments was due to the temperature of the fluid not having the right temperature and insufficient mixing of CO_2 and water before entering the core. The estimated error in temperature is 5 °C. To control theses errors I would recommend using a transfer vessel. This would allow the fluid to mix with CO_2 and to reach the right temperature for the experiment.
- A second recommendation would be to perform coreflood experiments in the micro CT scanner. At the moment the only way to get an idea of what is happening in the core is through the pressure that is measured at seven points along the core. It would be very interesting to get a visual representation of what is happening in the core and to study the behaviour of the exsolved CO_2 in the core. It would especially be interesting how the distribution of CO_2 is throughout the core and how relative permeability relates to the water/gas saturation and to see how this compares to imbibition and drainage experiments to see if drainage relative permeability experiments are applicable to the degassing process. With the degassing of CO_2 the free gas is in the form of

bubbles that are disconnected from one another while in drainage experiments the gas phase displaces the water phase and is connected (Zuo et al., 2011). The distribution of the gas phase is therefore different in these kind of experiments therefore there is no guarantee that widely available drainage relative permeability data can be used for to see how the presence of free gas influence the permeability when degassing occurs.

- In the six sets of experiments performed two types of cores were used, a Bentheimer and a Berea sandstone with a permeability of 2.3 and 0.14 Darcy respectively. These cores have different characteristics such as porosity, permeability and pore throat sizes. The rate at which the degassing process causes changes in effective permeability and the total effect on the effective permeability is also different. It would be interesting to use a third core with different characteristics to see if there is a relation between one or more of these characteristics and the effect of degassing process. The Delft Sandstone Member has two layers, the lower permeable one has a permeability comparable with the Berea sandstone core, the higher permeable one has a permeability between 0.6 and 1 Darcy (Donselaar et al., 2015). For a third core it would be interesting to use a core which is comparable to the higher permeable layer.
- Out of the 27 operational geothermal systems two operate from a limestone formation (EZK, 2021). With the ambitious geothermal goals which would require about 700 geothermal wells by the year 2050 (EBN, 2018) the geothermal potential of limestone formations can not be ignored. Therefore, it would be good to also do degassing experiments on limestone cores.

5.6. Implications

With the ambitious goals set out for the next decades for geothermal industry it is important acquire knowledge that can reduce potential technical risks. This research is focused on one of the risks related to the gases dissolved in fluids. Geothermal fluids often have a large amount of gasses and solids dissolved in them. As discussed in the theory, the pressure in a reservoir decreases rapidly near the wellbore during production which can cause gases to exsolve and negatively impact the permeability. This could have caused the productivity of the Gross Schönebeck to decrease. Downhole fluid sampling in this reservoir revealed the presence of free gas (Blocher et al., 2015). This research shows that the degassing of a fluid and therefore the presence of free gas negatively impacts the the permeability. The presence of free gas in the Gross Schönebeck together with the results from research make the idea the that degassing of fluid caused the decrease in permeability valid.

The formations which are a target for geothermal energy in the Dutch subsurface consists primarily out of sandstone (EZK, 2021). Therefore sandstone cores were used in this in this project. This results shows at which conditions the degassing process initiates and how this influences the permeability for different temperatures, pressures, CO_2 concentrations and for two different sandstone cores. This data is useful for the geothermal industry as it can help to predict whether degassing would take place for the conditions that apply to a reservoir and what the effect would be the permeability of the reservoir near the wellbore. For the successful management of geothermal projects the effect of the degassing of CO_2 due to changes in pressure near the wellbore should be incorporated to prevent unwelcome surprises. Besides recognizing the effect of degassing on the permeability effective management should also look at possible ways in which degassing can be avoided. The research has shown that degassing occurs due to a decrease in pressure near the wellbore. The key to preventing degassing from happening is to keep the pressure above the degassing pressure. Equation 2.11 shows that the pressure drawdown depends on multiple variables of which some are characteristics of the reservoir and therefore can not be changed. However, the rate at which the fluid is extracted from the reservoir is controllable. By managing the flow rate the pressure drawdown can be controlled to prevent the pressure to drop below the degassing pressure (Blocher et al., 2015).

What this research also shows is that the degassing process is reversible. With management the pressure drawdown can be limited and the pressure near the wellbore can be increased. This means that if degassing of fluid limits the water flow in a reservoir it can be reversed by managing the pressure drawdown.

6

Conclusion

The aim of this research was to asses at which conditions the degassing process would initiate for different conditions and what the effect of this process would be on the permeability of a reservoir. This was done by performing a series of coreflood experiments at different temperatures, CO_2 concentrations and pressures using two different sandstone cores. From the experiments the following conclusions can be drawn:

1. At temperatures of 30 °C and pressures between zero and 50 bar the maximum CO_2 concentration of Henry's law gives a good indication for when the degassing process starts. At higher temperatures Henry's law needs to be extrapolated using the Van 't Hoff equation to be applicable. The extrapolated Henry's law matches less with values obtained in the experiments with increasing temperature. This can be due the fluid in the core not reaching the right temperature or because of the values that are used to extrapolate Henry's law constant for different temperatures.

2. The effect of the degassing process on the effective permeability of a rock is largely influenced by the pore scale characteristics of a rock. Comparing a high permeable (2.3 Darcy) Bentheimer sandstone core with a lower permeable (0.14 Darcy) Berea sandstone core shows that the degassing process causes the effective permeability to reduce faster in the low permeable Berea core than in the Bentheimer core. The total decrease in the Berea core is also significantly higher than in the Bentheimer core, the reduction in effective permeability is 91% and 48% respectively. This difference is most likely due their difference in pore throat size distribution. The Berea has more small pore throats what causes them to block earlier because small bubbles already have the potential to block the pore throats while in the Bentheimer the small bubbles that form at the onset of the degassing process can still pass through the wider pore throats.

3. Using a 1M NaCl brine instead of tap water causes the degassing process to start at a higher pressure. It does not change how the degassing process alters the effective permeability. An increase in salinity causes the interfacial tension between brine and CO_2 to increase and therefore the capillary force. This increase however is not large enough to cause changes in the trapping of bubbles and on the effect of the degassing process on the effective permeability.

4. The degassing process and the effect of the process on the effective permeability can be reversed by increasing the pressure. To completely reverse the effective permeability to the initial value, the pressure has to increase to a higher value than the degassing pressure.

As discussed in section 2.5 the trapping of bubbles in a porous medium is largely controlled by pore throat radii, the bubble radii, and the two forces acting on a bubble when it is trapped. Both the temperature and the salinity influence the forces that act on a trapped pore. The effects of these two variables on the way the degassing process affects the effective permeability, however, is limited. By increasing the temperature the total decrease in effective permeability due to degassing went from 91% to 89% at 30 and 70 °C respectively. For an increase in salinity the change in effective permeability was negligible.

The most important factor determining the effect of the degassing process on the effective permeability are the pore scale characteristics. For the core with smaller pore throat sizes a small drop below the degassing pressure cause the effective permeability to reduce near instantly and the total decrease in effective permeability to be much larger.

The main implication lay in the operational management of geothermal projects. The research shows that the degassing process significantly reduces the effective permeability which is unfavorable for producing geothermal water from the subsurface. The conditions at which the degassing process are discussed in this research. Ones the conditions are known they can be avoided by managing the operations of geothermal projects.

Bibliography

[1] George Arfken. *University Physics*. Maarssen, Netherlands: Elsevier Gezondheidszorg, 2012.

[2] Stefán Arnórsson and Einar Gunnlaugsson. “New gas geothermometers for geothermal exploration—calibration and application”. In: *Geochimica et Cosmochimica Acta* 49.6 (1985), pp. 1307–1325. DOI: 10.1016/0016-7037(85)90283-2.

[3] J. Banaś et al. “Effect of CO2 and H2S on the composition and stability of passive film on iron alloys in geothermal water”. In: *Electrochimica Acta* 52.18 (2007), pp. 5704–5714. DOI: 10.1016/j.electacta.2007.01.086.

[4] Jacob Bear. *Dynamics of Fluids in Porous Media*. Dover, UK: Dover Publications, 2013.

[5] Guido Blöcher et al. “Hydraulic history and current state of the deep geothermal reservoir Groß Schönebeck”. In: *Geothermics* 63 (2016), pp. 27–43. DOI: 10.1016/j.geothermics.2015.07.008.

[6] John J. Carroll, John D. Slupsky, and Alan E. Mather. “The Solubility of Carbon Dioxide in Water at Low Pressure”. In: *Journal of Physical and Chemical Reference Data* 20.6 (1991), pp. 1201–1209. DOI: 10.1063/1.555900.

[7] Raymond Chang and John Thoman. *Physical Chemistry for the Chemical Sciences*. Amsterdam, Netherlands: Adfo Books, 2014.

[8] Pierre Chiquet et al. “CO2/water interfacial tensions under pressure and temperature conditions of CO2 geological storage”. In: *Energy Conversion and Management* 48.3 (2007), pp. 736–744. DOI: 10.1016/j.enconman.2006.09.011.

[9] G.K.W. Dawson et al. “Experimental mineral dissolution in Berea Sandstone reacted with CO 2 or SO 2 –CO 2 in NaCl brine under CO 2 sequestration conditions”. In: *Chemical Geology* 399 (2015), pp. 87–97. DOI: 10.1016/j.chemgeo.2014.10.005.

[10] M Donselaar, R Groenenberg, and D Gilding. “ Reservoir geology and geothermal potential of the delft sandstone member in the west Netherlands basin.” In: *Proceedings world geothermal congress.* (2015), pp. 1–9.

[11] EBN et al. *Masterplan Aardwarmte*. Tech. rep. May 2018.

[12] EZK, Ministerie van Economische zaken en Klimaat. *Jaarverslag 2020 delfstoffen en aardwarmte in Nederland*. Tech. rep. Aug. 2021.

[13] John R. Fanchi. “Measures of Rock-Fluid Interactions”. In: *Shared Earth Modeling* (2002), pp. 108–132. DOI: 10.1016/b978-075067522-2/50007-0.

[14] Hamid Reza Feili et al. “Risk analysis of geothermal power plants using Failure Modes and Effects Analysis (FMEA) technique”. In: *Energy Conversion and Management* 72 (2013), pp. 69–76. DOI: 10.1016/j.enconman.2012.10.027.

[15] J. Gong et al. “Laboratory Investigation of Liquid Injectivity in Surfactant-Alternating-Gas Foam Enhanced Oil Recovery”. In: *Transport in Porous Media* 131.1 (2019), pp. 85–99. DOI: 10.1007/s11242-018-01231-5.

[16] Linxian Gong, Lei Nie, and Yan Xu. “Geometrical and Topological Analysis of Pore Space in Sandstones Based on X-ray Computed Tomography”. In: *Energies* 13.15 (2020), p. 3774. DOI: 10.3390/en13153774.

[17] J. R. Haizlip et al. “Origin and Impacts of High Concentrations of Carbon Dioxide in Geothermal Fluids of Western Turkey”. In: Stanford, CA USA: Stanford, 2016.

[18] P. E. Jacobo. *GAS CHEMISTRY OF THE AHUACHAPÁN AND BERLÍN GEOTHERMAL FIELDS, EL SALVADOR*. Tech. rep. 12. Reykjavik, Iceland, 2003.

[19] Ralph Kühne, Ralf-Uwe Ebert, and Gerrit Schüürmann. “Prediction of the Temperature Dependency of Henry’s Law Constant from Chemical Structure”. In: *Environmental Science Technology* 39.17 (2005), pp. 6705–6711. DOI: 10.1021/es050527h.

[20] Kewen Li and Roland N. Horne. “Fractal modeling of capillary pressure curves for The Geysers rocks”. In: *Geothermics* 35.2 (2006), pp. 198–207. DOI: 10.1016/j.geothermics.2006.02.001.

[21] AS Al-Menhali and S Krevor. “Capillary Trapping of CO2in Oil Reservoirs: Observations in a Mixed-Wet Carbonate Rock”. In: *Environmental Science Technology* 50.5 (2016), pp. 2727–2734. DOI: 10.1021/acs.est.5b05925.

[22] G. Pátzay et al. “Modeling of scale formation and corrosion from geothermal water”. In: *Electrochimica Acta* 43.1-2 (1998), pp. 137–147. DOI: 10.1016/s0013-4686(97)00242-9.

[23] AE Peksa, KHA Wolf, and PL Zitha. “Bentheimer sandstone revisited for experimental purposes”. In: *Marine and Petroleum Geology* 67 (2015), pp. 701–719. DOI: 10.1016/j.marpetgeo.2015.06.001.

[24] C Pentland et al. “Immiscible Displacements and Capillary Trapping in CO2 Storage”. In: *Energy Procedia* 4 (2011), pp. 4969–4976. DOI: 10.1016/j.egypro.2011.02.467.

[25] J. F. PEPPER, W. DE WITT, and D. F. DEMAREST. “Geology of the Bedford Shale and Berea Sandstone in the Appalachian Basin”. In: *Science* 119.3094 (1954), pp. 512–513. DOI: 10.1126/science.119.3094.512-a.

[26] Mark S. Ramsey. “Pressure Drop Calculations”. In: *Practical Wellbore Hydraulics and Hole Cleaning* (2019), pp. 163–216. DOI: 10.1016/b978-0-12-817088-5.00005-8.

[27] Simona Regenspurg et al. “Geochemical properties of saline geothermal fluids from the in-situ geothermal laboratory Groß Schönebeck (Germany)”. In: *Geochemistry* 70 (2010), pp. 3–12. DOI: 10.1016/j.chemer.2010.05.002.

[28] R Sander. “Compilation of Henry’s law constants (version 4.0) for water as solvent”. In: *Atmospheric Chemistry and Physics* 15.8 (2015), pp. 4399–4981. DOI: 10.5194/acp-15-4399-2015.

[29] A Schumpe. “The estimation of gas solubilities in salt solutions”. In: *Chemical Engineering Science* 48.1 (1993), pp. 153–158. DOI: 10.1016/0009-2509(93)80291-w.

[30] Badar Al-Shakry et al. “Polymer Injectivity: Influence of Permeability in the Flow of EOR Polymers in Porous Media”. In: *Day 3 Wed, June 05, 2019* (2019). DOI: 10.2118/195495-ms.

[31] Mostafa H. Sharqawy, John H. Lienhard, and Syed M. Zubair. “Thermophysical properties of seawater: a review of existing correlations and data”. In: *Desalination and Water Treatment* 16.1-3 (2010), pp. 354–380. DOI: 10.5004/dwt.2010.1079.

[32] TNO. *Corrosion in Dutch geothermal systems*. Tech. rep. TNO 2015 R10160. Mar. 2016.

[33] UNFCCC. *Key aspects of the Paris Agreement*. 2021. URL: https://unfccc.int/process-and-meetings/the-paris-agreement/the-paris-agreement/key-aspects-of-the-paris-agreement.

[34] D Wildenschild et al. “Exploring capillary trapping efficiency as a function of interfacial tension, viscosity, and flow rate”. In: *Energy Procedia* 4 (2011), pp. 4945–4952. DOI: 10.1016/j.egypro.2011.02.464.

[35] Da-Qing Zheng, Tian-Min Guo, and Helmut Knapp. “Experimental and modeling studies on the solubility of CO2, CHC1F2, CHF3, C2H2F4 and C2H4F2 in water and aqueous NaCl solutions under low pressures”. In: *Fluid Phase Equilibria* 129.1-2 (1997), pp. 197–209. DOI: 10.1016/s0378-3812(96)03177-9.

[36] R.W. Zimmerman. *Imperial College Lectures In Petroleum Engineering, The - Volume 5: Fluid Flow In Porous Media*. Zaltbommel, Nederland: Van Haren Publishing, 2018.

[37] L Zuo et al. “An Experimental Study of CO2 Exsolution and Relative Permeability Measurements During CO2 Saturated Water Depressurization”. In: *Transport in Porous Media* 91.2 (2011), pp. 459–478. DOI: 10.1007/s11242-011-9854-2.

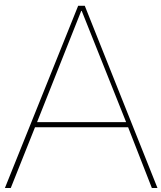

Dates and Parameters experiments

Table A.1: Dates and parameters of all experiments

Set	Experiment	date	CO_2 concentration	flow rate (mL/min	Pressure (Bar)	T (°C	Water
Set 1	1.1	23/03/2021		60	5.3	30	Tap
	1.2	26/03/2021		40	5.3	30	Tap
	1.3	30/03/2021		40	10	30	Tap
	1.4	01/04/2021		40	5.5	30	Tap
	1.5	19/05/2021		30	15.2	30	Tap
	1.6	20/05/2021		30	12	30	Tap
	1.7	21/05/2021		30	18	30	Tap
	1.8	02/06/2021		30	21.7	30	Tap
Set 2	2.1	30/04/2021	0.454	5		30	Tap
	2.2	04/05/2021	0.302	5		30	Tap
	2.3	04/05/2021	0.604	5		30	Tap
	2.4	07/05/2021	0.544	5		30	Tap
	2.5	11/05/2021	0.665	5		30	Tap
	2.6	26/05/2021	0.847	20		30	Tap
	2.7	26/05/2021	0.847	15		30	Tap
	2.8	27/05/2021	0.998	15		30	Tap
	2.9	28/05/2021	1.115	15		30	Tap
	2.10	28/05/2021	1.21	15		30	Tap
	2.11	01/06/2021	1.301	15		30	Tap
Set 3	3.1	17/06/2021	0.30	15		30	Tap
	3.2	17/06/2021	0.50	15		30	Tap
	3.3	23/06/2021	0.70	15		30	Tap
	3.4	23/06/2021	0.90	12		30	Tap
	3.5	24/06/2021	1.10	20		30	Tap
	3.6	24/06/2021	0.40	15		30	Tap
	3.7	24/06/2021	0.20	15		30	Tap
	3.8	25/06/2021	1.30	15		30	Tap
Set 4	4.1	29/06/2021	0.40	15		40	Tap
	4.2	30/06/2021	0.20	15		40	Tap
	4.3	01/07/2021	0.40	15		50	Tap
	4.4	01/07/2021	0.20	15		50	Tap
	4.5	06/07/2021	0.40	15		60	Tap
	4.6	07/07/2021	0.40	15		70	Tap
	4.7	08/07/2021	0.20	15		70	Tap
	4.8	09/07/2021	0.40	15		80	Tap
	4.9	14/07/2021	0.20	15		80	Tap
	4.10	09/07/2021	0.40	15		90	Tap
	4.11	13/07/2021	0.40	30		90	Tap
	4.12	14/07/2021	0.40	20		80	Tap
	4.13	22/07/2021	0.40	15		70	Tap
	4.14	09/09/2021	0.20	15		80	Tap
Set 5	5.1	06/08/2021	0.40	15		70	Tap
	5.2	13/08/2021	0.90	15		70	Tap
	5.3	18/08/2021	0.80	15		70	Tap
	5.4	08/09/2021	0.60	15		70	Tap
Set 6	6.1	24/08/2021	0.40	15		70	Brine
	6.2	24/08/2021	0.20	15		70	Brine
	6.3	25/08/2021	0.60	15		70	Brine
	6.4	26/08/2021	0.80	10		70	Brine
	6.5	31/08/2021	0.80	15		70	Brine

B

Increase pressure drop over first interval core

During the experiments performed on the Berea sandstone core there was an continuing increase in the pressure drop over the first interval of the core, closest to the inlet. This increase in pressure drop over this interval made to assume that this interval was getting clogged. For the results of this research the focus was not on this interval. The focus in this research was on the last interval, closest to the outlet of the core. Experiments that were repeated with several weeks or months in between them show no difference in results. Therefore, this increase in pressure drop over the first interval can be neglected for the results of this research.